Fractures and faults across intrusion-induced forced folds: a georesource perspective

[1]Craig Magee

[1]School of Earth and Environment, University of Leeds, UK

Running title: Intrusion-induced forced folds and fractures

Abstract

Intruding magma can create space by uplift and elastic bending of the overburden, which locally fractures the deforming volume and produces dome-like forced folds. Due to their geometry and fracture network, such intrusion-induced forced folds make ideal fluid traps. As these forced folds are common in many volcanic settings and sedimentary basins, they present exploration targets for water, magmatic-related mineral and metal deposits, and CO_2 storage. Here, I map fracture networks and quantify their geometry and connectivity across a range of natural and modelled intrusion-induced forced folds. I show that there is a strong relationship between forced fold length and amplitude, and all fracture networks comprise traces with variable lengths and orientations, and are more intense and denser where fold curvature is greatest. Fracture length populations are typically best described by power-law distributions, but some fit better to log-normal or exponential distributions. Connectivity of fracture networks is low and generally increases with folding, but resurfacing by eruptive products can disrupt this trend. My work supports previous analyses of forced folds and fractures, suggesting that their geometries may not be diagnostic of the fold driver. We can thus use exposed forced folds to help predict fracture characteristics of buried forced folds.

Supplementary material: text or .svg files containing co-ordinate information of fracture vertices for input into FracPaQ are available at XXXX.

Introduction

Space for the emplacement of tabular magma bodies (sills and laccoliths), particularly at shallow-levels, is commonly created by uplift of the overlying rock and free surface (e.g. Pollard and Johnson 1973; Segall 2013). This uplift bends the overburden to produce dome-like forced folds, within which localised extension and compression along outer- and inner-arcs, respectively, drives internal deformation (Fig. 1a) (e.g. Pollard and Johnson 1973; Magee *et al.* 2013; Wilson *et al.* 2021); these forced folds are similar to periclinal folds generated above faults or salt bodies, and by differential compaction (e.g. Stearns 1978; Cosgrove and Hillier 1999; Lisle 1999; Meng and Hodgetts 2020). Like these other types of four-way dip closure, intrusion-induced forced folds in sedimentary basins have been targeted for petroleum exploration, with some found to host hydrocarbon reserves (e.g. Schutter 2003; Rodriguez Monreal *et al.* 2009; Jackson *et al.* 2020). As intrusion-induced forced folds can thus trap fluids, it is worth considering their suitability as potential targets for water, geothermal, or mineral/metal exploration, as well as CO_2 storage (e.g. Weis 2012; Scott *et al.* 2015; Montanari *et al.* 2017; Wilson *et al.* 2021).

Drivers of forced folding have limited lateral extents and underlie the deforming rock volume, meaning elastic bending dictates fold development as opposed to buckling, which involves (sub-)horizontal compression (e.g. Pollard and Johnson 1973; Cosgrove and Ameen 1999; Goulty and Schofield 2008). This bending occurs radially about a central point or axis, producing a non-developable surface fold with non-zero Gaussian curvature (e.g. a dome); most buckle folds form developable surfaces (Figs 1a and b) (e.g. Lisle 1999; Mynatt *et al.*

2007). Being a non-developable surface means forced fold growth induces radial and circumferential tension along outer-arcs, locally instigating internal fracturing and normal faulting of the bending rock volume (Figs 1a and c) (e.g. Stearns 1978; Cosgrove and Ameen 1999). These tensional stresses become compressional in inner-arc sections, where deformation bands and compaction may occur (Figs 1a and c) (e.g. Ramsey 1968; Pollard and Johnson 1973; Wilson *et al.* 2021). Critically, the development of tensional and compressional structures within a rock volume can markedly change its porosity and permeability, influencing fluid flow (e.g. Fossen and Bale 2007; Sanderson and Nixon 2015; Dimmen *et al.* 2020). Yet few studies have explored how bending-related deformation within intrusion-induced forced folds may affect fluid flow (e.g. Wilson *et al.* 2021). To assess the suitability of intrusion-induced forced folds as potential exploration or storage targets, for a variety of fluids critical to the energy transition, we need to constrain how their deformation history impacts porosity and permeability (Wilson *et al.* 2021).

Here, I build on previous work examining fracture development in forced folds (Cosgrove and Ameen 1999; Pearce *et al.* 2011; Cosgrove 2015; Wilson *et al.* 2021) by analysing fracture networks across the top surface of intrusion-induced forced folds. Specifically, I use satellite imagery and bathymetry data to map faults and fractures across: (1) long-lived forced folds within the Erta'Ale Volcanic Segment, in the Danakil Depression sedimentary basin, Ethiopia (Magee *et al.* 2017); and (2) at Cordón Caulle (Chile) and West Mata (Lau Basin, SW Pacific), where recent individual intrusion events produced new forced folds (e.g. Castro *et al.* 2016; Chadwick Jr *et al.* 2019). I compare these mapped fold and fracture geometries to forced folds recognised in seismic reflection data (Hansen and Cartwright 2006) and generated in physical experiments (Montanari *et al.* 2017; Henriquet *et al.* 2019; Poppe *et al.* 2019; Montanari *et al.* 2020; Warsitzka *et al.* 2022). With these data, I aim to constrain fracture network characteristics of intrusion-induced forced folds. This work will help inform predictions of subsurface fracture networks within forced folds, and contribute to the assessment of forced folds in georesource exploration and storage.

Case studies

Erta'Ale Volcanic Segment

Situated in the Danakil Depression, a Pleistocene–Recent sedimentary basin comprising a thick sequence of evaporites, the Erta'Ale Volcanic Segment (EAVS) marks one of the final phases of continental break-up along the Red Sea rift (Fig. 2a) (e.g. Bastow *et al.* 2018). The EAVS contains a series of volcanoes surrounded by basaltic to silicic lavas, which primarily emanate from fissures oriented NW-SE (Fig. 2a) (e.g. Watts *et al.* 2020). Spatially associated with several volcanoes in the EAVS are dome-like features that are heavily fractured and faulted: (1) the Alu and Alu South domes are close to and partially underlie the composite Dalafilla stratovolcano, respectively (Fig. 2b) (Pagli *et al.* 2012; Magee *et al.* 2017); (2) adjacent to the Borale'Ale stratovolcano is a sub-circular dome, previously interpreted to be a shield volcano, containing an elliptical central graben that itself hosts a small volcanic vent (Fig. 2c) (Barberi and Varet 1970; Watts *et al.* 2020); and (3) a broad area of uplift beneath the Gada'Ale volcano (referred to as Gada'Ale East) associated with an adjacent, complex dome (referred to as Gada'Ale West), both of which are inferred to be formed due to underlying salt movement (Fig. 2d) (Barberi and Varet 1970). Another dome-like structure is present ~30 km north of the EAVS at the Dallol volcano (Fig. 2e) (e.g. López-García *et al.* 2020). Mapping of lava flows that deflect around these domes suggest they formed over the past <80 Kyr (e.g. Fig. 2b) (Magee *et al.* 2017; Watts *et al.* 2020). Ground deformation geodetically detected at these sites, except Borale'Ale, over the past 35 years indicates the domes continue to periodically uplift and subside, likely linked to subsurface magmatism (Amelung *et al.* 2000; Nobile *et al.* 2012; Pagli *et al.* 2012; Albino and Biggs 2021). For example, a 23.2×10^6 m^3 lava eruption from a NW-trending fissure ~2 km NW of the Dalafilla stratovolcano summit in 2008 was: (1) preceded by ~9 cm of uplift across Alu over three months; and (2) accompanied by ~1.9 m and ~1 m of subsidence at the Alu and Alu South domes, respectively (Pagli *et al.* 2012). Modelling of this ground deformation suggest Alu and Alu South are underlain by a sill at 1 km depth, possibly with a saucer-shaped geometry, and a larger magma reservoir at 4 km (Pagli *et al.* 2012; Magee *et al.* 2017). Based on their morphology and relation to magmatic or slat movement events, it is plausible that these dome-like features at Alu, Alu South, Borale'Ale, Gada'Ale, and Dallol are forced folds (Barberi and Varet 1970; Magee *et al.* 2017).

Cordón Caulle

On 4th June 2011, the rhyolitic volcano Cordón Caulle, Southern Chile, produced an explosive sub-Plinian eruption followed by lava effusion beginning on 15th June (Fig. 3a) (e.g. Castro *et al.* 2016; Wadsworth *et al.* 2022). Between the ~8th June and 3rd July 2011, surface elevations in a ~12 km^2 area around the vent site increased by up to ~240 m; these elevation changes can partly be attributed to eruption of a ~35– 60 m thick lava, but primarily relate to intrusion-induced surface uplift of previous tephra layers (i.e. forced folding; Fig. 3a) (Castro *et al.* 2016). Modelling this ground deformation suggests uplift was driven by emplacement of a laccolith, with a 0.8–2 km radius and ~0.8 km^3 volume, at a depth of 20–200 m and pressure of 1–10 MPa (Castro *et al.* 2016). Development of the forced fold was accompanied by surface fracturing and faulting (Fig. 3a) (e.g. Castro *et al.* 2016; Wadsworth *et al.* 2022). Subsidence of up to 40 m occurred across the forced fold from August 2011 onwards, and has been related to magma migration out of the laccolith (perhaps coupled with thermal contraction) (Zheng *et al.* 2020) or sintering of pyroclasts during intrusion growth (Wadsworth *et al.* 2022).

West Mata

The West Mata submarine volcano is located between the NE Lau Spreading Centre and the Tofua Volcanic Arc near Fiji and Samoa in the SW Pacific (Fig. 3b) (Chadwick Jr *et al.* 2019). Towards the NE of the volcano base, bathymetric depths decreased by up to 64 m across a 0.73 x 10^6 m^2 area over some period between 2012 and 2016 (Chadwick Jr *et al.* 2019). Part of this depth change can be attributed to emplacement of lava from a NE-SW trending fissure, but most relates to uplift of seafloor sediments and creation of a dome (forced fold) bisected by numerous fractures (Fig. 3b) (Chadwick Jr *et al.* 2019).

'Fold B'

Seismic reflection data reveal 'Fold B' is a dome-shaped forced fold, 3.5 km in diameter and up to ~250 m high, developed ~1 km above a 3 x 2.5 km, up to ~300 m thick, saucer-shaped sill (Hansen and Cartwright 2006; their Fig. 4). This sill-fold pair is situated in the NE Rockall Basin and formed in the Late Paleocene-to-Early Eocene within a siliciclastic sedimentary succession (Hansen and Cartwright 2006). A series of normal faults cross-cut the forced fold (Hansen and Cartwright 2006; their Fig. 10).

Methodology

I use Google Earth and ArcGIS Pro World imagery of different vintages to map potential forced folds and linear features across them in the EAVS and at Cordón Caulle, at a resolution of ~30 m (Figs 2 and 3a). For West Mata, I use high-resolution (~1 m) bathymetry data collected using a multibeam sonar system on the AUV *Sentry* during part of a two-leg expedition by the *R/V Falkor* crew in 2017 (Fig. 3b) (Chadwick Jr *et al.* 2019). The 3D seismic reflection survey (T38) used to map 'Fold B' has a vertical and horizontal resolution of up to ~68 m, if we consider each is equivalent to a quarter of the seismic wavelength (λ/4) (Hansen and Cartwright 2006; Brown 2011). I also generate fold and fracture maps for physical experiments using select published images (see Supplementary Material) (Montanari *et al.* 2017; Henriquet *et al.* 2019; Poppe *et al.* 2019; Montanari *et al.* 2020; Warsitzka *et al.* 2022).

Where fold outlines could be confidently identified in the remote sensing data and model images, I measure fold length, width, and map-view area (A). I also measure fold amplitudes where elevation data, or cross-sections through the folds, are available; for these measurements, I assume that the pre-fold datum follows the regional trend of the current free surface outboard of the fold outline (e.g. Figs 1a and c). However, there are some uncertainties in the measurement of forced fold length and amplitude: (1) we can rarely establish the original surface topography prior to emplacement and folding, so often cannot accurately constrain true amplitudes; (2) syn- or post-emplacement deposition of sediments or resurfacing by lavas may alter apparent forced fold heights or regional base levels (e.g. Dobb *et al.* 2022; Warsitzka *et al.* 2022); (3) fold crests may have been eroded (e.g. Hansen and Cartwright 2006); and/or (4) measurements from 2D seismic reflection data, which are rarely depth-converted and decompacted (Magee *et al.* 2019), or physical model cross-sections may not intersect forced fold maximum amplitude or length (e.g. Jackson *et al.* 2013).

For the EAVS forced folds, available Shuttle Radar Topography Mission (SRTM) 1 Arc-second global data allow me to measure their current surface area (A_i). Comparing the map-view and current surface area measurements of the EAVS forced folds provides an estimate of the extensional strain across the fold tops. The SRTM data also allow me to calculate the Gaussian curvature (K; Fig. 1b) of the EAVS folds by extracting a point cloud grid, with spacings of 30 m, for import into the PyVvista module for Python (Sullivan and

Kaszynski 2019); forced folds elsewhere were not analysed with this method as their respective data were not in suitable formats. PyVista takes the X, Y, Z co-ordinate data of the point cloud to create a mesh (Sullivan and Kaszynski 2019), and then calculates the Gaussian curvature of each node from their principal curvatures (k_1, k_2; Fig. 1b) (Lisle 1999).

I interpret linear features recognised across the studied forced folds as fractures and faults, but acknowledge some may be related to fluvial incision (e.g. Henriquet *et al.* 2019), gravitational collapse, and/or processing artefacts; without ground-truthing, the fracture maps cannot be validated. Although some linear features mapped may thus not relate to extension during folding, I note that: (1) fractures can focus fluvial incision, meaning mapped channels may be a proxy for fracture locations (Henriquet *et al.* 2019); and (2) gravitational processes could affect the long-term distribution of fractures in folds. From the mapped fractures and faults, I use FracPaQ software to analyse their network properties, such as trace and segment line length and strike, fracture intensity and density, and connectivity (Fig. 4) (Healy *et al.* 2017). Because the entire traces of all resolved fractures are mapped across the forced folds, no adjustments are required to account for fractures extending beyond study limits. Deriving fracture trace and segment length distributions is critical predicting fracture network attributes at smaller or larger scales (e.g. Rizzo *et al.* 2017). In FracPaQ, these distributions are statistically analysed using Maximum Likelihood Estimators (MLE), which establishes the probability of whether the data is best-fit by power-law, log-normal, or exponential distributions (Healy *et al.* 2017; Rizzo *et al.* 2017). Fracture intensity (P21) describes the total fracture length in set area, whereas fracture density (P20) measures the number of fractures in the same area (Healy *et al.* 2017); these parameters were calculated using a circular scan window method (Healy *et al.* 2017), but only assessed for natural forced folds because the number of fractures created in modelled forced folds is generally too low to be statistically meaningful. As Gaussian curvature is a measure of 3D strain, fracture intensity and density should increase where K is greatest (Lisle 1999). To assess network connectivity, FracPaQ identifies I-, Y-, and X-nodes of fractures, whereby I-nodes correspond to isolated fracture tips, Y-nodes occur where one fracture abuts another, and X-nodes where fractures cross-cut each other (Fig. 4) (Sanderson and Nixon 2015; Healy *et al.* 2017). All node maps obtained from FracPaQ were manually verified and adjusted where needed. From the number of these nodes ($N_{I,Y,X}$) per forced fold, I calculate the number of lines bound by I- and Y-nodes (N_L), the number of branches (N_B) defining portions of fractures bound by any two nodes, the average number of connections per line (C_L), and the average number of branches per line (C_B) (Sanderson and Nixon 2015):

$$N_L = 0.5(N_I + N_Y)$$

$$N_B = 0.5(N_I + 3N_Y + 4N_X)$$

$$C_L = 2(N_Y + N_X)/N_L$$

$$C_B = (3N_Y + 4N_X)/N_B$$

Both C_L and C_B are useful indicators of connectivity (Sanderson and Nixon 2015; Healy *et al.* 2017). For example, simulated percolation of randomly oriented lines of a fixed length occurs at $C_L = 3.57$ (Sanderson and Nixon 2015).

Results

The studied natural forced folds are circular to elliptical, with length to width aspect ratios of ~1.00–2.05, and they have amplitudes, lengths, and map areas that range from ~40–368 m, ~0.9–4.1 km, and ~0.27–16.01 km^2, respectively (Figs 2-3 and 5-6; Table 1). For those in the EAVS, comparison of map-view area and current surface area measurements suggests the top of the forced folds have increased in size by 0.1–4.97% during uplift (Table 1). There is a moderate, positive power-law relationship between fold length and maximum amplitude of most these natural forced folds (R^2 = 0.51), but this fit decreases if the Dallol forced fold is included (R^2 = 0.13) (Fig. 7). Other forced folds show similar length to amplitude relationships, akin to published lengths and thicknesses of sub-horizontal tabular intrusions (Fig. 7). For forced folds produced in physical models (Fig. 8; Table 2), there also appears to be a moderate, positive power-law relationship between the fold length and amplitude (R^2 = 0.66) where this data is available (Fig. 7). The power-law fit between all natural and modelled fold lengths and amplitudes is strong (R^2 = 0.89) and positive, regardless of whether Dallol is included or not (Fig. 7).

The fractures and their constituent segments mapped along the top of the natural forced folds vary in number and length (Figs 5-6 and 9-10; Table 1). Segment numbers and total trace length are particularly low for the seismically imaged 'Fold B' (253 segments totalling 2.376 km long), compared to those mapped in satellite or bathymetry data, for which 758–4160 segments are mapped that total trace lengths are ~13.4–114.6 km (Figs 5 and 10; Table 1). Within each natural forced fold, there is typically a relatively reduced amount of fracture traces or segments at small length fractions, particularly for 'Fold B' (Figs 9-10). The probability that the length distributions of these fracture populations describe log-normal, power-law, or exponential relationships are often similar, but: (1) the probability that trace or segment lengths define power-law distributions are always >95%; and (2) for some forced folds, the probability that trace and segment lengths define a log-normal (e.g. Alu South) or exponential (e.g. Gada'Ale West) distribution are relatively low (<80%) (Figs 9-10; Table 3). There is a moderate, positive power-law relationship between fold area and total trace length of the natural forced folds excluding 'Fold B' (R^2 = 0.55), and those physical models where these geometry parameters are reported (R^2 = 0.60); the power-law fit between the natural (excluding 'Fold B') and model forced folds is strong (R^2 = 0.99) (Fig. 11; Tables 1-2).

The fracture networks, including those observed across modelled forced folds, typically show a broad range of strike orientations, although many contain fracture populations preferentially oriented sub-parallel to the fold long axes (Figs 5-6 and 8). Fracture distributions are also variable across individual forced folds (Figs 5-6 and 8); e.g. fracture intensity and density typically appear greatest where major normal faults are developed (e.g. in Borale'Ale) and/or Gaussian curvature is highest (Figs 5-6). The connectivity of the studied fracture systems in natural forced folds is low (C_L <1.31 and C_B <1.17), being dominated by I-nodes and containing <10% X-nodes (Figs 5-6 and 12a; Table 2). Connectivity of fracture networks produced within modelled forced folds is also typically low but does increase up to C_L values of 3.01 and C_B values of 1.66 (Fig. 12A; Table 3). Where physical models provide constraints on how fracture networks developed through time, it is clear that connectivity generally increases via the proportional formation of more Y- and X-nodes following power-law (e.g. SPCTIN06; $R^2 = 0.78$) or exponential (e.g. Exp1B; $R^2 = 0.80$) relationships (Fig. 12). However, decreases in connectivity can occur when eruptions resurface the folds (e.g. Fig. 13).

Discussion

As the four-way dip closure form of intrusion-induced forced folds can trap fluids (e.g. Schutter 2003; Rodriguez Monreal *et al.* 2009), and these structures are present in many sedimentary basins and active volcanic settings worldwide (e.g. Pollard and Johnson 1973; Holford *et al.* 2012; van Wyk de Vries *et al.* 2014; Magee *et al.* 2016; Magee *et al.* 2017; Tian *et al.* 2021; Kumar *et al.* 2022), we should consider them as potential fluid storage sites. For example, their association with magmatism means intrusion-induced forced folds may trap hydrothermal fluids, creating: (1) suitable geothermal energy exploration targets in active volcanic settings (e.g. Scott *et al.* 2015; Montanari *et al.* 2017); or (2) important mineral/metal accumulations, such as porphyry copper deposits (e.g. Weis 2012). Similarly, ancient intrusion-induced forced folds may host aquifers (e.g. Wilson *et al.* 2021), or could potentially provide suitable CO_2 storage sites (cf. Tueckmantel *et al.* 2012). Critically, forced folding involves bending of a rock volume, which locally induces internal fracturing and faulting, thereby modifying permeability (e.g. Jackson and Pollard 1990; Cosgrove and Ameen 1999; Wilson *et al.* 2021). These changes in permeability can enhance the fluid storage potential of these traps, but can leading to breaching and fluid leakage (see Cosgrove 2015 and references therein). To appraise whether intrusion-induced forced folds may provide suitable fluid storage sites, we need to establish how their evolution affects fracture connectivity, which controls host rock permeability (e.g. Sanderson and Nixon 2015; Wilson *et al.* 2021). Furthermore, because most intrusion-induced forced fold exploration targets will be in the subsurface, we will lack direct information on the geometry or growth of their fracture network. Stochastic models are thus required to simulate potential fracture patterns and their impact on fluid flow, which themselves need to be underpinned by statistical characterisation of natural fracture networks (e.g. Riley 2005).

Intrusion-induced forced folding and fracturing

Emplacement of tabular magma bodies at shallow-levels commonly drives roof uplift, producing dome-like forced folds bisected by extensional fracture and normal fault networks (e.g. Pollard and Johnson 1973; Magee *et al.* 2013; Segall 2013; van Wyk de Vries *et al.* 2014; Magee *et al.* 2017). There is a strong, positive relationship ($R^2 = 0.89$) between forced fold length and maximum amplitude, broadly consistent with reported lengths and thicknesses of tabular intrusions (Fig. 7) (see also Magee *et al.* 2017 and references therein). In addition to this geometrical similarity, the fracture networks the studied forced folds all contain fractures and faults of variable orientation and length, which increase in intensity and density with fold curvature (Figs 5-6 and 8; Table 1). Previous studies examining fracturing across periclinal folds associated with other forced folding mechanisms also describe similar fracture networks characteristics (e.g. Stearns 1978; Cosgrove and Ameen 1999; Lisle 1999; Cosgrove 2015). These findings support other works showing that it is the behaviour of the deforming rock volume during bending, itself a function of lithology, size of the forcing feature, and strain rate, which primarily controls forced folding and fracturing (e.g. Pollard and Johnson 1973; Stearns 1978; Gholipour *et al.* 2016). The similarity between intrusion-induced forced folds (e.g. Alu, Alu South, Cordón Caulle, and West Mata) (Pagli *et al.* 2012; Castro *et al.* 2016; Magee *et al.* 2017; Chadwick Jr *et al.* 2019) and the Gada'Ale East and West domes, which have been attributed to underlying salt movement (Barberi and Varet 1970), could thus be interpreted as evidence that: (1) the Gada'Ale folds formed in response to magma (and salt?) movement, consistent with recognition of recent dyke-related uplift near Gada'Ale East (Amelung *et al.* 2000); or (2) the geometry and fracturing of dome-like folds is not diagnostic of their driving mechanism. Overall, it thus seems that the geometry and growth of fracture networks during bending is largely independent from the mechanism driving folding, implying we could use exposed intrusion-induced forced folds to benchmark fracture network prediction of those in the subsurface (e.g. Gholipour *et al.* 2016).

Fracture length distribution

The fracture length distribution of a sample set is often used to predict fracture network characteristics at smaller and/or larger scales (e.g. Bonnet *et al.* 2001). By using a robust statistical approach to assess probability of fit to different distributions (Rizzo *et al.* 2017), I show that most intrusion-induced forced folds contain fracture networks with trace and segment lengths compatible with a power-law relationship (Figs 9-10; Table 3). Yet it should be noted that for some datasets, log-normal (e.g. Dallol segment lengths) or exponential (e.g.

Alu trace lengths) distributions appear more probable fits (Table 3). A limitation with this analysis is that the resolution of the data may mean short fracture traces or segments are undersampled (Figs 9-10), which can cause power-law distributions to appear log-normal (Bonnet *et al.* 2001).

Fracture connectivity

My data reveal that the connectivity of fracture networks across the tops of natural and modelled forced folds tends to remain relatively low (C_L <3.01 and C_B <1.66; Fig. 12; Tables 1-2) (see Sanderson and Nixon 2015 and references therein). These results contrast with field-based analyses of a forced monocline above the Trachyte Mesa intrusion, Utah, which show fractures and deformation bands are locally well-connected (Wilson *et al.* 2021). There are several possible reasons for these disparities in fracture connectivity. Firstly, the remote sensing and seismic reflection data I use to analyse natural forced folds have limited resolutions of metres to tens of metres (e.g. Hansen and Cartwright 2006). It is thus plausible that unidentified fractures may be present, or identified fractures extend further, at scales below these data resolutions, which could lead to an increase in connectivity (e.g. Nixon *et al.* 2012). Secondly, my study distils a connectivity value for the entire top surface of each forced fold, obscuring zones where connectivity may locally be enhanced due to relatively higher fracture intensity, density, and/or fold curvature (e.g. Lisle 1999; Wilson *et al.* 2021); future work should focus on partitioning intrusion-induced forced folds, likely based on variations in curvature, to further assess connectivity patterns. Finally, I analysed fracture patterns on the top surface of forced folds, whereas the analyses of Trachyte Mesa examined fractures and deformation bands expressed on rock walls that form a cross-section through the forced fold (Wilson *et al.* 2021); i.e. my work provides some insight into the lateral connectivity of intrusion-induced forced fold fracture networks, but Wilson *et al.* (2021)

provide a robust assessment of vertical connectivity. Overall, comparing our work demonstrates that ground-truthing is ideally required to test remotely determined connectivity of fracture networks (Wilson *et al.* 2021). Furthermore, it will be crucial to establish how connectivity varies in 3D across entire forced folds (Wilson *et al.* 2021), which will require integrating analyses of well-exposed forced folds and those imaged in 3D seismic reflection data.

An opportunity for CO_2 storage?

Successful sequestration of CO_2 through *in situ* mineral carbonation in basaltic rocks has opened up lava fields and volcanoes as potential exploration targets for CO_2 storage (e.g. Matter *et al.* 2016; Holford *et al.* 2021; Raza *et al.* 2022; Fedorik *et al.* 2023). This method typically relies on injection of either water and dissolved CO_2, or supercritical CO_2, into basalts that the fluids react with to permanently fix CO_2 in carbonate minerals (e.g. McGrail *et al.* 2014; Snæbjörnsdóttir *et al.* 2020). Permeability of the basalts is thus key as it enables fluid flow away from injection sites, and increases the surface area of the rock that fluids can react with (e.g. Fedorik *et al.* 2023). Basalt lavas often contain a variety of fracture sets (e.g. cooling joints) and porosity (e.g. Snæbjörnsdóttir *et al.* 2018; Holford *et al.* 2021), but I those within intrusion-induced forced folds (e.g. in the EAVS) will contain additional fracture sets due to bending-related stresses. Given forced folds can also form suitable fluid traps, if reservoirs and seals are in place, it seems reasonable that those containing basaltic lava flows may form suitable CO_2 storage targets.

Conclusions

Intrusion-induced forced folds commonly contain an array of fractures generated by bending-related stresses during uplift. Coupled with the dome-like geometry of these forced folds, the presence of complex fracture networks suggests they may form suitable pathways and traps for fluid flow. By comparing natural forced folds developed recently and those produced in physical experiments, I show that there is: (1) a positive relationships between forced fold length and amplitude; (2) fracture networks comprise traces and segments with variable lengths, predominantly conforming to power-law distributions, and orientations; (3) fracture intensity and density generally increases with fold curvature and/or the presence of major normal faults; and (4) connectivity across the top of forced folds appears relatively low, but this may be due to limitations in the resolution of the data used. Fold and fracture development appear to be largely independent of the mechanism driving uplift, instead being related to the behaviour of the deforming rock during bending; we can thus use forced folds at the surface to inform predictions regarding fracturing of subsurface forced folds if they share similar host rock geology. Critically, intrusion-induced forced folds should be considered as exploration targets in the search for water aquifers, geothermal potential, and minerals/metals. Fracturing induced by bending may also increase the permeability of lavas within forced folds, potentially enhancing their suitability for CO_2 storage.

Acknowledgements

I am grateful to funding from a NERC Independent Research Fellowship (NE\R014086\1).

Author contributions

CM designed and conducted the analyses, and wrote the manuscript.

Data availability statement

All satellite and bathymetry data used is available through either ArcGIS Pro, Google Earth, EarthExplorer (https://earthexplorer.usgs.gov/), or the Marine Geoscience Data System (https://www.marine-geo.org/tools/search/DataSets.php?data_set_uids=24446,24447). Seismic reflection and physical model data are published, with some of the images used taken from associated supplementary files. The vertices of fractures mapped in this work are provided as text or .svg files, ready for import into FracPaQ, in the Supplementary Material. Any other data is provided in the Figures and Tables.

Figure captions

Figure 1: (a) Schematic of a forced fold developed above an inflating sill or laccolith, highlighting areas where outer-arc and circumferential extension occur, and inner-arc compression. The pre-fold datum marks the original surface prior to folding. (b) Cartoons showing how buckling creates folds that can typically be described as a developable surface, whereby one of the principal curvatures (k_1, k_2) is zero, meaning the Gaussian curvature (K) is also zero. In contrast, uplift driven by forced folding creates a non-developable surface with non-zero Gaussian curvature (modified from Lisle 1999). (c) Seismic reflection image from the Glencoe 3D survey offshore NW Australia depicting a forced fold above a thick sill (same sill as studied by Dobb *et al.* 2022). Field photograph showing forced folding above the dioritic Trachyte Mesa intrusion in the Henry Mountains, Utah. The sandstone beds thin across the fold due to bending-related porosity reduction (Morgan *et al.* 2008).

Figure 2: (a) Satellite image of the Erta'Ale Volcanic Segment (EAVS) within the Danakil Depression, Ethiopia, highlighting volcanoes and areas of exposed evaporites. Inset elevation map from the TopoBathy Elevation Tinted Hillshade available through ArcGIS Pro. (b-f) Oblique Google Earth views of the (potential) forced folds studied here: Alu (Image © 2022 CNES / Airbus, Image © 2022 Maxar Technologies; Imagery date: 12/16/2018), Alu South (Image © 2022 CNES / Airbus, Image © 2022 Maxar Technologies, Image Landsat /

Copernicus Imagery date: 10/17/2019), Borale'Ale (Image Landsat / Copernicus, Image © 2022 Maxar Technologies, Imagery date: 02/19/2011), Gada'Ale East and West Image (Landsat / Copernicus, Image © 2022 CNES / Airbus, Imagery date: 12/16/2018), and Dallol (Image Landsat / Copernicus, Image © 2022 CNES / Airbus, Imagery date: 02/26/2019).

Figure 3: (a) Google Earth imagery of the Cordón Caulle forced fold, from before and after its development. (b) Bathymetry map of the forced fold developed at West Mata, and a map showing the change in depth across the fold and surrounding lava flow (modified from Chadwick Jr *et al.* 2019). Inset elevation maps for (a-b) from the TopoBathy Elevation Tinted Hillshade available through ArcGIS Pro.

Figure 4: Schematic showing fracture trace and segment definition, as well as I-, Y-, and X-node characterisation.

Figure 5: Compilation of maps for the EAVS forced folds highlighting their elevation (SRTM data) and fracture patterns. Copernicus Sentinel-2 imagery data [2015] retrieved from ArcGIS Pro, processed by ESA. Maps of fracture segment strike (with associated rose diagrams where n is the number of segments), density, and intensity are also provided, along with fracture connectivity. Gaussian curvature is also shown.

Figure 6: Compilation of maps for Cordón Caulle, West Mata, and 'Fold B' showing their fracture segment strike (with associated rose diagrams where n is the number of segments), density, intensity, and connectivity.

Figure 7: Plot of fold length and amplitude for the studied forced folds, including those

created in physical models where this information is provided or can be extracted (see Tables 1-2 for data). Forced fold and tabular intrusion measurements for other studies are also shown (data collated by and presented in Magee *et al.* 2017).

Figure 8: Segment strike sand fracture connectivity maps of the physical model forced folds studied. All maps show the fracture networks at their most developed. No experiment duration is provided for the Henriquet *et al.* (2019) models, but the timestamp of other models is shown in seconds (s).

Figure 9: Frequency histograms, cumulative frequency plots, and Maximum Likelihood Estimator probability (Pr) charts of fracture trace length for the natural forced folds studied. The probability charts test the fit of the data to a log-normal, power-lar, or exponential distribution (see Table 4). *n* is the number of fracture traces mapped.

Figure 10: Frequency histograms, cumulative frequency plots, and Maximum Likelihood Estimator probability (Pr) charts of fracture segment length for the natural forced folds studied. The probability charts test the fit of the data to a log-normal, power-lar, or exponential distribution (see Table 3). *n* is the number of fracture traces mapped.

Figure 11: Plot of forced fold area and total fracture trace length (see Tables 1-2 for data).

Figure 12: (a) Ternary diagrams showing the proportion of I-, Y-, and X-nodes for each forced fold compared to contours showing the number of connections per line (C_L). Where images of modelled forced folds were acquired at different timestamps, the evolution of connectivity can be constrained. (b) Plot of connectivity against the normalised time for

Exp1B and Exp2B (Warsitzka *et al.* 2022) and SPCTIN06 (Poppe *et al.* 2019), showing its evolution can be described by power-law or exponential relationships. Reductions in connectivity may be attributed to resurfacing of the forced fold by erupted products (see Fig. 13).

Figure 13: Model photograph and fracture map of Exp2B showing fractures developed 4662 seconds (s) into the experiment are partly covered by erupted material at 4700 s (Warsitzka *et al.* 2022).

References

Albino, F. and Biggs, J. 2021. Magmatic processes in the East African Rift system: insights from a 2015–2020 Sentinel-1 InSAR survey. *Geochemistry, Geophysics, Geosystems*, **22**, e2020GC009488.

Amelung, F., Oppenheimer, C., Segall, P. and Zebker, H. 2000. Ground deformation near Gada ‘Ale Volcano, Afar, observed by radar interferometry. *Geophys. Res. Lett*, **27**, 3093-3096.

Barberi, F. and Varet, J. 1970. The Erta Ale volcanic range (Danakil depression, northern afar, ethiopia). *Bulletin Volcanologique*, **34**, 848-917.

Bastow, I.D., Booth, A.D. *et al.* 2018. The Development of Late-Stage Continental Breakup: Seismic Reflection and Borehole Evidence from the Danakil Depression, Ethiopia. *Tectonics*, **37**, 2848-2862.

Bonnet, E., Bour, O., Odling, N.E., Davy, P., Main, I., Cowie, P. and Berkowitz, B. 2001. Scaling of fracture systems in geological media. *Reviews of Geophysics*, **39**, 347-383.

Brown, A.R. 2011. *Interpretation of three-dimensional seismic data*. 6th ed. AAPG and SEG, Oklahoma, USA.

Castro, J.M., Cordonnier, B., Schipper, C.I., Tuffen, H., Baumann, T.S. and Feisel, Y. 2016. Rapid laccolith intrusion driven by explosive volcanic eruption. *Nature communications*, **7**, 13585, https://doi.org/10.1038/ncomms13585 http://www.nature.com/articles/ncomms13585#supplementary-information.

Chadwick Jr, W.W., Rubin, K.H., Merle, S.G., Bobbitt, A.M., Kwasnitschka, T. and Embley, R.W. 2019. Recent eruptions between 2012 and 2018 discovered at west mata submarine volcano (NE Lau Basin, SW Pacific) and characterized by new ship, AUV, and ROV data. *Frontiers in Marine Science*, 495.

Cosgrove, J. 2015. The association of folds and fractures and the link between folding, fracturing and fluid flow during the evolution of a fold–thrust belt: a brief review. *Geological Society, London, Special Publications*, **421**, 41-68.

Cosgrove, J.W. and Ameen, M.S. 1999. A comparison of the geometry, spatial organization and fracture patterns associated with forced folds and buckle folds. *Geological Society, London, Special Publications*, **169**, 7-21, https://doi.org/10.1144/gsl.sp.2000.169.01.02.

Cosgrove, J.W. and Hillier, R.D. 1999. Forced-fold development within Tertiary sediments of the Alba Field, UKCS: evidence of differential compaction and post-depositional sandstone remobilization. *Geological Society, London, Special Publications*, **169**, 61-71, https://doi.org/10.1144/gsl.sp.2000.169.01.05.

Dimmen, V., Rotevatn, A. and Nixon, C.W. 2020. The relationship between fluid flow, structures, and depositional architecture in sedimentary rocks: An example-based overview. *Geofluids*, **2020**, 1-19.

Dobb, E.M., Magee, C., Jackson, C.A.-L., Lathrop, B. and Köpping, J. 2022. Impact of igneous intrusion and associated ground deformation on the stratigraphic record. *Geological Society, London, Special Publications*, **525**, SP525-2021-2115.

Fedorik, J., Delaunay, A.J.R. *et al.* 2023. Structure and fracture characterization of the Jizan group: Implications for subsurface CO2 basalt mineralization. *Frontiers in Earth Science*, **10**, https://doi.org/https://doi.org/10.3389/feart.2022.946532.

Fossen, H. and Bale, A. 2007. Deformation bands and their influence on fluid flow. *AAPG Bulletin*, **91**, 1685-1700.

Gholipour, A.M., Cosgrove, J.W. and Ala, M. 2016. New theoretical model for predicting and modelling fractures in folded fractured reservoirs. *Petroleum Geoscience*, **22**, 257-280.

Goulty, N.R. and Schofield, N. 2008. Implications of simple flexure theory for the formation of saucer-shaped sills. *Journal of Structural Geology*, **30**, 812-817, https://doi.org/10.1016/j.jsg.2008.04.002.

Hansen, D.M. and Cartwright, J. 2006. The three-dimensional geometry and growth of forced folds above saucer-shaped igneous sills. *Journal of Structural Geology*, **28**, 1520-1535, https://doi.org/10.1016/j.jsg.2006.04.004.

Healy, D., Rizzo, R.E. *et al.* 2017. FracPaQ: A MATLAB™ toolbox for the quantification of fracture patterns. *Journal of Structural Geology*, **95**, 1-16.

Henriquet, M., Dominguez, S., Barreca, G., Malavieille, J., Cadio, C. and Monaco, C. 2019. Deep origin of the dome-shaped Hyblean Plateau, southeastern Sicily: A new tectono-magmatic model. *Tectonics*, **38**, 4488-4515.

Holford, S., Schofield, N., Bunch, M., Bischoff, A. and Swierczek, E. 2021. Storing CO2 in buried volcanoes. *The APPEA Journal*, **61**, 626-631.

Holford, S.P., Schofield, N., MacDonald, J.D., Duddy, I.R. and Green, P.F. 2012. Seismic analysis of igneous systems in sedimentary basins and their impacts on hydrocarbon prospectivity: examples from the southern Australian margin. *APPEA Journal*, **52**, 23.

Jackson, C.A.-L., Schofield, N. and Golenkov, B. 2013. Geometry and controls on the development of igneous sill–related forced folds: A 2-D seismic reflection case study from offshore southern Australia. *Geological Society of America Bulletin*, **125**, 1874-1890, https://doi.org/10.1130/b30833.1.

Jackson, C.A.-L., Magee, C. and Jacquemyn, C. 2020. Rift-related magmatism influences petroleum system development in the NE Irish Rockall Basin, offshore Ireland. *Petroleum Geoscience*, **26**, 511-524.

Jackson, M.D. and Pollard, D.D. 1990. Flexure and faulting of sedimentary host rocks during growth of igneous domes, Henry Mountains, Utah. *Journal of Structural Geology*, **12**, 185-206.

Kumar, P.C., Niyazi, Y., Eruteya, O.E., Moscariello, A., Warne, M., Ierodiaconou, D. and Sain, K. 2022. Anatomy of intrusion related forced fold in the offshore Otway Basin, SE Australia. *Marine and Petroleum Geology*, **141**, 105719.

Lisle, R.J. 1999. Predicting patterns of strain from three-dimensional fold geometries: neutral surface folds and forced folds. *Geological Society, London, Special Publications*, **169**, 213-221, https://doi.org/10.1144/gsl.sp.2000.169.01.16.

López-García, J.M., Moreira, D., Benzerara, K., Grunewald, O. and López-García, P. 2020. Origin and evolution of the halo-volcanic complex of Dallol: proto-volcanism in Northern Afar (Ethiopia). *Frontiers in Earth Science*, 351.

Magee, C., Briggs, F. and Jackson, C.A.-L. 2013. Lithological controls on igneous intrusion-induced ground deformation. *Journal of the Geological Society*, **170**, 853-856, https://doi.org/10.1144/jgs2013-029.

Magee, C., Hoggett, M., Jackson, C.A.-L. and Jones, S.M. 2019. Burial-Related Compaction Modifies Intrusion-Induced Forced Folds: Implications for Reconciling Roof Uplift Mechanisms Using Seismic Reflection Data. *Frontiers in Earth Science*, **7**, https://doi.org/10.3389/feart.2019.00037.

Magee, C., Bastow, I.D., de Vries, B.v.W., Jackson, C.A.-L., Hetherington, R., Hagos, M. and Hoggett, M. 2017. Structure and dynamics of surface uplift induced by incremental sill emplacement. *Geology*, **45**, 431-434.

Magee, C., Muirhead, J.D. *et al.* 2016. Lateral magma flow in mafic sill complexes. *Geosphere*, **12**, 809-841.

Matter, J.M., Stute, M. *et al.* 2016. Rapid carbon mineralization for permanent disposal of anthropogenic carbon dioxide emissions. *Science*, **352**, 1312-1314.

McGrail, B.P., Spane, F.A., Amonette, J.E., Thompson, C. and Brown, C.F. 2014. Injection and monitoring at the Wallula basalt pilot project. *Energy Procedia*, **63**, 2939-2948.

Meng, Q. and Hodgetts, D. 2020. Forced folding and fracturing induced by differential compaction during post-depositional inflation of sandbodies: insights from numerical modelling. *Marine and Petroleum Geology*, **112**, 104052.

Montanari, D., Del Ventisette, C. and Bonini, M. 2020. Lateral magma migration through interconnected sills: Evidence from analogue modeling. *Earth and Planetary Science Letters*, **551**, 116568.

Montanari, D., Bonini, M., Corti, G., Agostini, A., Del Ventisette, C.J.J.o.V. and Research, G. 2017. Forced folding above shallow magma intrusions: Insights on supercritical fluid flow from analogue modelling. **345**, 67-80.

Morgan, S., Stanik, A., Horsman, E., Tikoff, B., de Saint Blanquat, M. and Habert, G. 2008. Emplacement of multiple magma sheets and wall rock deformation: Trachyte Mesa intrusion, Henry Mountains, Utah. *Journal of Structural Geology*, **30**, 491-512, https://doi.org/10.1016/j.jsg.2008.01.005.

Mynatt, I., Bergbauer, S. and Pollard, D.D. 2007. Using differential geometry to describe 3-D folds. *Journal of Structural Geology*, **29**, 1256-1266.

Nixon, C.W., Sanderson, D.J. and Bull, J.M. 2012. Analysis of a strike-slip fault network using high resolution multibeam bathymetry, offshore NW Devon UK. *Tectonophysics*, **541**, 69-80.

Nobile, A., Pagli, C., Keir, D., Wright, T.J., Ayele, A., Ruch, J. and Acocella, V. 2012. Dike-fault interaction during the 2004 Dallol intrusion at the northern edge of the Erta Ale Ridge (Afar, Ethiopia). *Geophysical Research Letters*, **39**.

Pagli, C., Wright, T.J., Ebinger, C.J., Yun, S.-H., Cann, J.R., Barnie, T. and Ayele, A. 2012. Shallow axial magma chamber at the slow-spreading Erta Ale Ridge. *Nature Geoscience*, **5**, 284-288.

Pearce, M.A., Jones, R.R., Smith, S.A. and McCaffrey, K.J. 2011. Quantification of fold curvature and fracturing using terrestrial laser scanning. *AAPG Bulletin*, **95**, 771-794.

Pollard, D.D. and Johnson, A.M. 1973. Mechanics of growth of some laccolithic intrusions in the Henry Mountains, Utah, II: bending and failure of overburden layers and sill formation. *Tectonophysics*, **18**, 311-354.

Poppe, S., Holohan, E.P. *et al.* 2019. An Inside Perspective on Magma Intrusion: Quantifying 3D Displacement and Strain in Laboratory Experiments by Dynamic X-Ray Computed Tomography. **7**, 62.

Ramsey, J.G. 1968. *Folding and fracturing of rock*. The Blackburn Press, New Jersey.

Raza, A., Glatz, G., Gholami, R., Mahmoud, M. and Alafnan, S. 2022. Carbon mineralization and geological storage of CO2 in basalt: Mechanisms and technical challenges. *Earth-Science Reviews*, **229**, 104036.

Riley, M.S. 2005. Fracture trace length and number distributions from fracture mapping. *Journal of Geophysical Research: Solid Earth*, **110**.

Rizzo, R.E., Healy, D. and De Siena, L. 2017. Benefits of maximum likelihood estimators for fracture attribute analysis: Implications for permeability and up-scaling. *Journal of Structural Geology*, **95**, 17-31.

Rodriguez Monreal, F., Villar, H., Baudino, R., Delpino, D. and Zencich, S. 2009. Modeling an atypical petroleum system: a case study of hydrocarbon generation, migration and accumulation related to igneous intrusions in the Neuquen Basin, Argentina. *Marine and Petroleum Geology*, **26**, 590-605.

Sanderson, D.J. and Nixon, C.W. 2015. The use of topology in fracture network characterization. *Journal of Structural Geology*, **72**, 55-66.

Schutter, S.R. 2003. Hydrocarbon occurrence and exploration in and around igneous rocks. *Geological Society, London, Special Publications*, **214**, 7-33, https://doi.org/10.1144/gsl.sp.2003.214.01.02.

Scott, S., Driesner, T. and Weis, P. 2015. Geologic controls on supercritical geothermal resources above magmatic intrusions. *Nature communications*, **6**, 7837.

Segall, P. 2013. Volcano deformation and eruption forecasting. *Geological Society, London, Special Publications*, **380**.

Snæbjörnsdóttir, S.Ó., Sigfússon, B., Marieni, C., Goldberg, D., Gislason, S.R. and Oelkers, E.H. 2020. Carbon dioxide storage through mineral carbonation. *Nature Reviews Earth and Environment*, **1**, 90-102.

Snæbjörnsdóttir, S.Ó., Tómasdóttir, S. *et al.* 2018. The geology and hydrology of the CarbFix2 site, SW-Iceland. *Energy Procedia*, **146**, 146-157.

Stearns, D.W. 1978. Faulting and forced folding in the Rocky Mountains foreland. *Geological Society of America Memoirs*, **151**, 1-38.

Sullivan, C. and Kaszynski, A. 2019. PyVista: 3D plotting and mesh analysis through a streamlined interface for the Visualization Toolkit (VTK). *Journal of Open Source Software*, **4**, 1450.

Tian, W., Li, X. and Wang, L. 2021. Forced fold amplitude and sill thickness constrained by wireline and 3-D seismic data suggest an elastic magma-induced deformation in Tarim Basin, NW China. *Minerals*, **11**, 293.

Tueckmantel, C., Fisher, Q.J., Manzocchi, T., Skachkov, S. and Grattoni, C.A. 2012. Two-phase fluid flow properties of cataclastic fault rocks: Implications for CO2 storage in saline aquifers. *Geology*, **40**, 39-42.

van Wyk de Vries, B., Márquez, A., Herrera, R., Bruña, J.G., Llanes, P. and Delcamp, A. 2014. Craters of elevation revisited: forced-folds, bulging and uplift of volcanoes. *Bulletin of Volcanology*, **76**, 1-20.

Wadsworth, F.B., Llewellin, E.W. *et al.* 2022. A reappraisal of explosive–effusive silicic eruption dynamics: syn-eruptive assembly of lava from the products of cryptic fragmentation. *Journal of Volcanology and Geothermal Research*, **432**, 107672.

Warsitzka, M., Kukowski, N. and May, F. 2022. Patterns and Failure Modes of Fractures Resulting From Forced Folding of Cohesive Caprocks–Comparison of 2D vs. 3D and Single- vs. Multi-Layered Analog Experiments. Front. *Frontiers in Earth Science*, **10**, 881134.

Watts, E.J., Gernon, T.M. *et al.* 2020. Evolution of the Alu-Dalafilla and Borale volcanoes, Afar, Ethiopia. *Journal of Volcanology and Geothermal Research*, **408**, 107094.

Weis, P. 2012. The dynamic interplay between saline fluid flow and rock permeability in magmatic–hydrothermal systems. *Geofluids*, 373-392.

Wilson, P.I., Wilson, R.W., Sanderson, D.J., Jarvis, I. and McCaffrey, K.J. 2021. Analysis of deformation bands associated with the Trachyte Mesa intrusion, Henry Mountains, Utah:

implications for reservoir connectivity and fluid flow around sill intrusions. *Solid Earth*, **12**, 95-117.

Zheng, W., Pritchard, M., Delgado, F. and Reath, K. 2020. Laccolith evolution during and after the 2011-12 eruption of Cordon Caulle volcano, Chile, from satellite feature-tracking, elevation, and thermal observations. *AGU Fall Meeting Abstracts*, V004-0025.

Table 1: *Natural forced fold geometry and fracture networks*

Location	Forced fold geometry								Total fracture length	Fracture connectivity							
	Length	Width	Length: width	Map area	Surface area	Strain	Maximum amplitude	Length: amplitude		I	Y	X	N_L	N_B	N_L/N_B	C_L	C_B
	(km)	(km)		(km^2)	(km^2)	(%)	(m)		(km)								
Alu	3.44	2.05	1.68	05.07	05.32	4.97	341	010.09	070.43	1755	275	17	1015	1324	1.30	0.58	0.67
Alu South	6.78	3.39	2.00	16.01	16.36	2.22	320	021.20	062.95	1166	129	16	0648	0809	1.25	0.45	0.56
Borale'Ale	4.99	4.11	1.22	15.27	15.63	2.41	368	013.57	037.77	0174	008	11	0091	0121	1.33	0.42	0.56
Gada'Ale East	4.27	3.83	1.11	13.50	11.52	1.97	366	011.66	068.66	2146	371	30	1259	1690	1.34	0.64	0.73
Gada'Ale West	4.46	3.70	1.20	11.30	13.61	0.82	180	024.78	114.56	0806	191	10	0499	0710	1.42	0.81	0.86
Dallol	5.51	3.29	1.68	11.70	11.71	0.10	040	137.79	035.49	0384	112	50	0248	0460	1.85	1.31	1.17
Cordón Caulle	2.13	1.80	1.18	02.99	-†	-	200	010.67	046.23	1313	360	18	0837	1233	1.47	0.90	0.93
West Mata	0.90	0.44	2.05	00.27	-	-	064	013.99	013.44	0343	134	05	0239	0383	1.60	1.17	1.10
'Fold B'	3.50	3.50	1.00	13.00	-	-	250	014.00	002.37	0103	022	00	0063	0085	1.35	0.70	0.78

† indicates measurements could not be acquired from available data

Table 2: *Modelled forced fold geometry and fracture networks*

Reference	Model	Time	Forced fold geometry						Total fracture length	Fracture connectivity							
			Length	Width	Length: width	Area	Maximum amplitude	Length: amplitude		I	Y	X	N_L	N_B	N_L/N_B	C_L	C_B
		(s)	(cm)	(cm)		(cm^2)	(cm)		(km)								
Henriquet et al. (2019)	Inherited basement faults	?*	368.48	293.11	1.26	0848.28	17.000	01.26	02.45	036	07	00	022	029	1.33	0.65	0.74
	No structural inheritance	?	456.84	440.83	1.04	1581.71	33.000	01.04	10.69	245	75	30	160	295	1.84	1.31	1.17
Montanari et al. (2017)	IMG04	?	-†	-	-	-	-	-	00.10	010	02	00	006	008	1.33	0.67	0.75
		?	075.53	071.03	1.06	0042.13	-	-	00.49	117	22	00	070	092	1.32	0.63	0.72
		?	074.36	069.15	1.08	0040.39	-	-	00.75	168	43	04	106	157	1.48	0.89	0.93
		?	093.47	079.75	1.17	0058.55	-	-	01.34	147	73	03	110	189	1.72	1.38	1.22
		2700	096.92	088.58	1.09	0067.42	00.800	12.11	01.38	129	97	05	113	220	1.95	1.81	1.41
	IMG05	?	057.20	050.79	1.13	0022.82	-	-	00.54	110	39	03	075	120	1.60	1.13	1.08
		?	060.02	054.26	1.11	0025.58	-	-	00.85	129	51	08	090	157	1.74	1.31	1.18
		?	069.77	062.01	1.13	0033.98	-	-	01.02	109	52	07	081	147	1.82	1.47	1.26
		2700	071.70	066.70	1.08	0037.56	01.000	07.17	00.89	106	51	67	079	264	3.36	3.01	1.60
Montanari et al. (2020)	IMG12	?	-	-	-	-	-	-	00.10	006	00	00	003	003	1.00	0.00	0.00
		?	-	-	-	-	-	-	00.42	019	02	01	011	015	1.38	0.57	0.69
		5400	168.20	-	-	-	00.719	23.39	00.73	036	14	01	025	041	1.64	1.20	1.12
	IMG14	?	108.66	104.71	1.04	0089.36	-	-	00.43	004	00	00	002	002	1.00	0.00	0.00
		?	165.76	105.84	1.57	0137.80	-	-	00.61	007	01	00	004	005	1.25	0.50	0.60
		5400	168.70	105.36	1.60	0139.59	00.670	25.18	00.73	015	01	00	008	009	1.13	0.25	0.33
	IMG15	5400	215.95	096.21	2.24	0163.18	00.980	22.04	01.70	094	22	02	058	084	1.45	0.83	0.88
Poppe et al. (2017)	SPCTIN06	0420	-	-	-	-	-	-	00.15	010	03	00	007	010	1.46	0.92	0.95
		0840	-	-	-	-	-	-	00.43	022	15	00	019	034	1.81	1.62	1.34
		1260	-	-	-	-	-	-	00.56	020	22	00	021	043	2.05	2.10	1.53
		1680	-	-	-	-	-	-	00.76	021	23	03	022	051	2.32	2.36	1.59
		2100	-	-	-	-	-	-	01.00	026	38	03	032	076	2.38	2.56	1.66
Warsitzka et al. (2022)	Experiment 1B	4400	-	-	-	-	-	-	00.01	004	00	00	002	002	1.00	0.00	0.00
		4500	-	-	-	-	-	-	00.04	006	00	00	003	003	1.00	0.00	0.00
		4600	-	-	-	-	-	-	00.05	006	00	00	003	003	1.00	0.00	0.00
		4700	-	-	-	-	-	-	00.07	004	00	00	002	002	1.00	0.00	0.00
		4800	-	-	-	-	-	-	00.10	006	00	00	003	003	1.00	0.00	0.00
		4900	-	-	-	-	-	-	00.12	008	00	00	004	004	1.00	0.00	0.00
		5000	-	-	-	-	-	-	00.12	006	01	00	004	005	1.29	0.57	0.67
		5100	-	-	-	-	-	-	00.13	008	01	00	005	006	1.22	0.44	0.55
		5200	-	-	-	-	-	-	00.13	010	01	00	006	007	1.18	0.36	0.46
		5300	-	-	-	-	-	-	00.18	019	03	00	011	014	1.27	0.55	0.64
		5400	-	-	-	-	-	-	00.18	021	03	00	012	015	1.25	0.50	0.60
		5500	-	-	-	-	-	-	00.22	022	04	00	013	017	1.31	0.62	0.71
		5600	-	-	-	-	-	-	00.23	028	04	00	016	020	1.25	0.50	0.60
		5700	-	-	-	-	-	-	00.28	026	04	00	015	019	1.27	0.53	0.63
		5800	-	-	-	-	-	-	00.28	026	04	00	015	019	1.27	0.53	0.63
		5900	-	-	-	-	-	-	00.29	024	04	00	014	018	1.29	0.57	0.67
		6000	-	-	-	-	-	-	00.32	026	04	00	015	019	1.27	0.53	0.63
		6100	-	-	-	-	-	-	00.35	025	05	00	015	020	1.33	0.67	0.75
		6200	-	-	-	-	-	-	00.36	023	05	00	014	019	1.36	0.71	0.79
		6300	-	-	-	-	-	-	00.42	024	06	00	015	021	1.40	0.80	0.86
		6400	-	-	-	-	-	-	00.44	025	07	00	016	023	1.44	0.88	0.91
		6500	-	-	-	-	-	-	00.45	019	07	00	013	020	1.54	1.08	1.05
		6600	-	-	-	-	-	-	00.47	019	09	00	014	023	1.64	1.29	1.17
		6700	-	-	-	-	-	-	00.50	015	09	00	012	021	1.75	1.50	1.29
		6800	-	-	-	-	-	-	00.61	016	12	00	014	026	1.86	1.71	1.38
		6834	-	-	-	-	-	-	00.83	021	17	00	019	036	1.89	1.79	1.42
	Experiment 2B	3800	-	-	-	-	-	-	00.01	002	00	00	001	001	1.00	0.00	0.00
		3900	-	-	-	-	-	-	00.11	006	00	00	003	003	1.00	0.00	0.00
		4000	-	-	-	-	-	-	00.14	004	00	00	002	002	1.00	0.00	0.00
		4100	-	-	-	-	-	-	00.20	005	01	00	003	004	1.33	0.67	0.75
		4200	-	-	-	-	-	-	00.21	003	01	00	002	003	1.50	1.00	1.00
		4300	-	-	-	-	-	-	00.32	004	02	00	003	005	1.67	1.33	1.20
		4400	-	-	-	-	-	-	00.33	004	02	00	003	005	1.67	1.33	1.20
		4500	-	-	-	-	-	-	00.48	010	04	00	007	011	1.57	1.14	1.09
		4600	-	-	-	-	-	-	01.13	026	12	01	019	033	1.74	1.37	1.21
		4662	-	-	-	-	-	-	01.51	032	23	01	028	053	1.91	1.75	1.39
		4700	-	-	-	-	-	-	01.27	034	12	01	023	037	1.61	1.13	1.08

*no information available. Henriquet et al. (2019) do not state duration, and Montanari et al. (2017, 2022) images are from videos with no timestamps.

† indicates measurements could not be acquired from available images

Table 3: *Maximum Likelihood Estimation of fracture length distribution*

Location	Probability fracture trace lengths conform to defined distribution			Probability fracture segment lengths conform to defined distribution		
	Log-normal (%)	Power-law (%)	Exponential (%)	Log-normal (%)	Power-law (%)	Exponential (%)
Alu	88.12	99.48	99.88	96.28	99.40	98.20
Alu South	73.92	98.92	99.64	86.28	95.72	99.72
Borale Ale	98.88	99.56	99.64	03.80	98.12	97.36
Gada East	98.68	99.88	50.44	91.68	97.04	96.36
Gada West	89.60	98.72	11.32	98.56	98.16	98.72
Dallol	99.00	99.84	99.76	98.60	97.36	74.40
Cordon	99.28	99.32	77.40	73.84	98.68	97.72
West Mata	98.88	99.64	94.72	98.92	98.20	98.96
'Fold B'	98.04	98.00	99.32	95.60	99.76	99.56

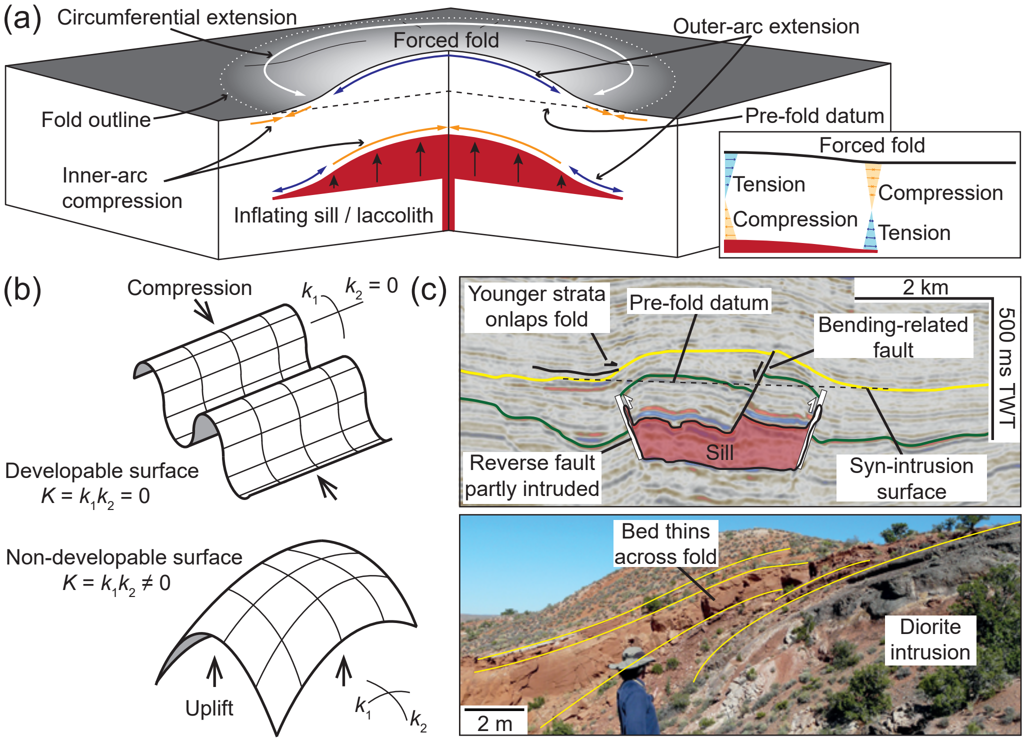
(a)
Circumferential extension
Forced fold
Outer-arc extension
Fold outline
Pre-fold datum
Inner-arc
compression
Inflating sill / laccolith
Forced fold
Tension
Compression
Compression
Tension
(b)
Compression
k_1
$k_2 = 0$
Developable surface
$K = k_1 k_2 = 0$
Non-developable surface
$K = k_1 k_2 \neq 0$
Uplift
k_1
k_2
(c)
Younger strata
onlaps fold
Pre-fold datum
2 km
Bending-related
fault
500 ms TWT
Sill
Reverse fault
partly intruded
Syn-intrusion
surface
Bed thins
across fold
Diorite
intrusion
2 m

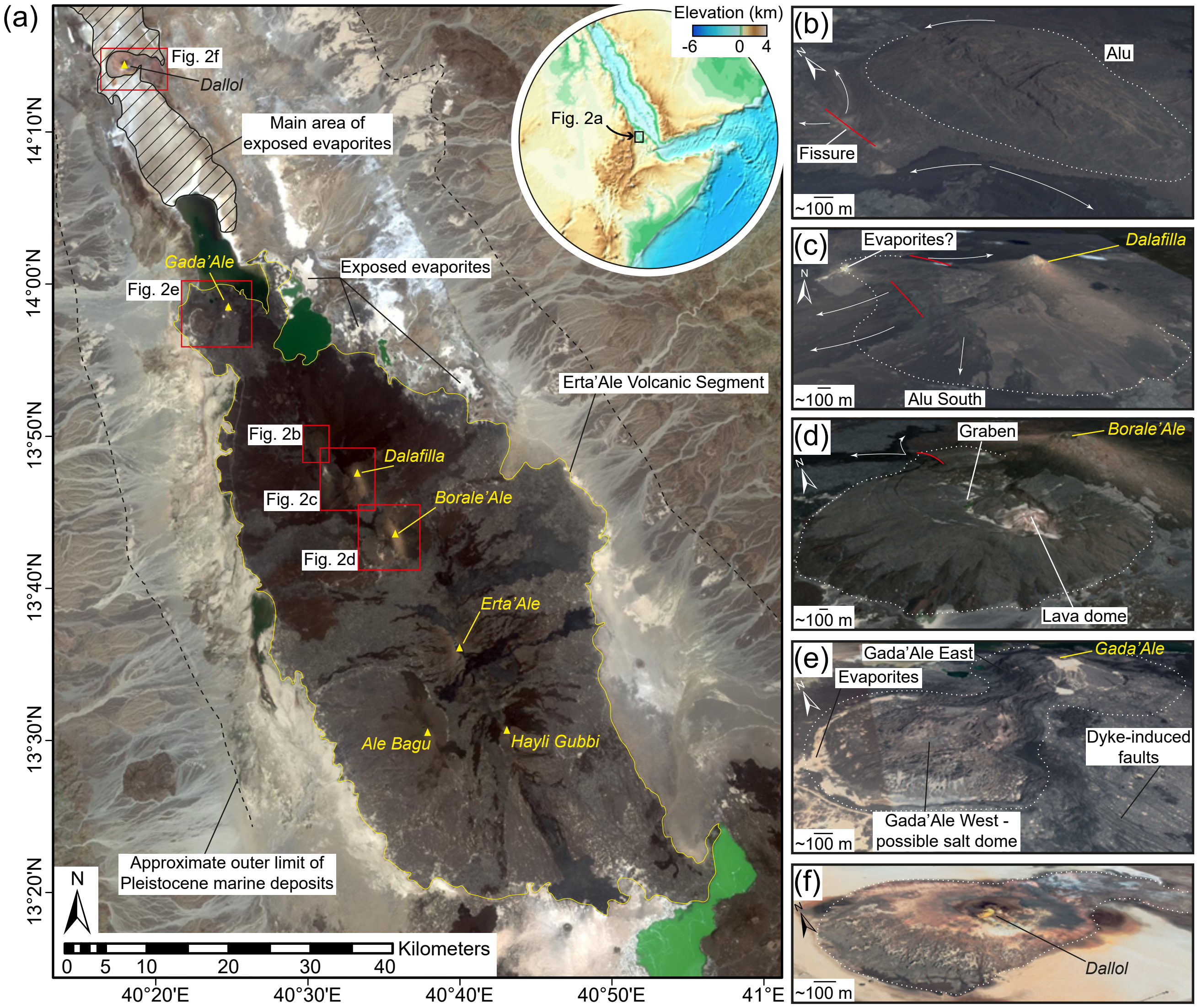

(a)
Elevation (km)
-6
0
4
Fig. 2a
Fig. 2f
Dallol
Main area of exposed evaporites
Gada'Ale
Fig. 2e
Exposed evaporites
Erta'Ale Volcanic Segment
Fig. 2b
Dalafilla
Fig. 2c
Borale'Ale
Fig. 2d
Erta'Ale
Ale Bagu
Hayli Gubbi
Approximate outer limit of Pleistocene marine deposits
N
0 5 10 20 30 40 Kilometers
14°10'N
14°00'N
13°50'N
13°40'N
13°30'N
13°20'N
40°20'E
40°30'E
40°40'E
40°50'E
41°E
(b)
Alu
Fissure
~100 m
(c)
Evaporites?
Dalafilla
Alu South
~100 m
(d)
Graben
Borale'Ale
Lava dome
~100 m
(e)
Gada'Ale East
Gada'Ale
Evaporites
Dyke-induced faults
Gada'Ale West - possible salt dome
~100 m
(f)
Dallol
~100 m

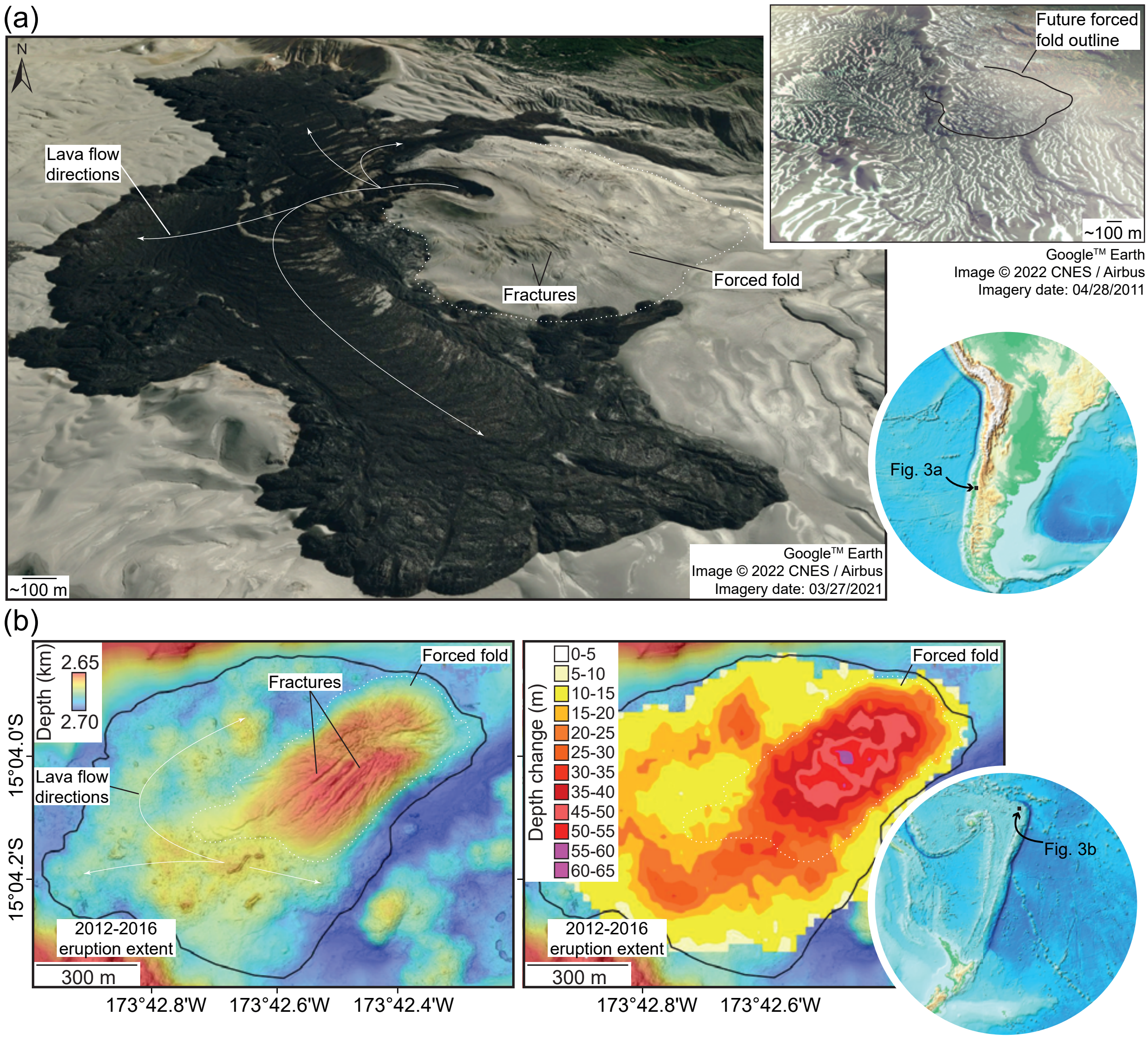
(a)
N
Lava flow directions
Fractures
Forced fold
~100 m
Google™ Earth
Image © 2022 CNES / Airbus
Imagery date: 03/27/2021
Future forced fold outline
~100 m
Google™ Earth
Image © 2022 CNES / Airbus
Imagery date: 04/28/2011
Fig. 3a
(b)
Depth (km)
2.65
2.70
Fractures
Forced fold
Lava flow directions
15°04.0'S
15°04.2'S
2012-2016 eruption extent
300 m
173°42.8'W
173°42.6'W
173°42.4'W
Depth change (m)
0-5
5-10
10-15
15-20
20-25
25-30
30-35
35-40
45-50
50-55
55-60
60-65
Forced fold
2012-2016 eruption extent
300 m
173°42.8'W
173°42.6'W
Fig. 3b

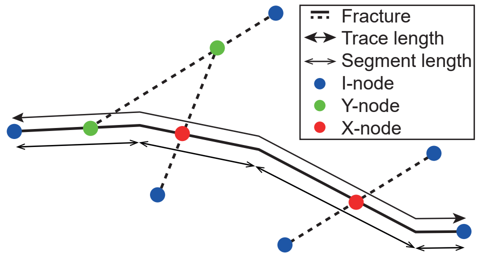

Fracture
Trace length
Segment length
I-node
Y-node
X-node

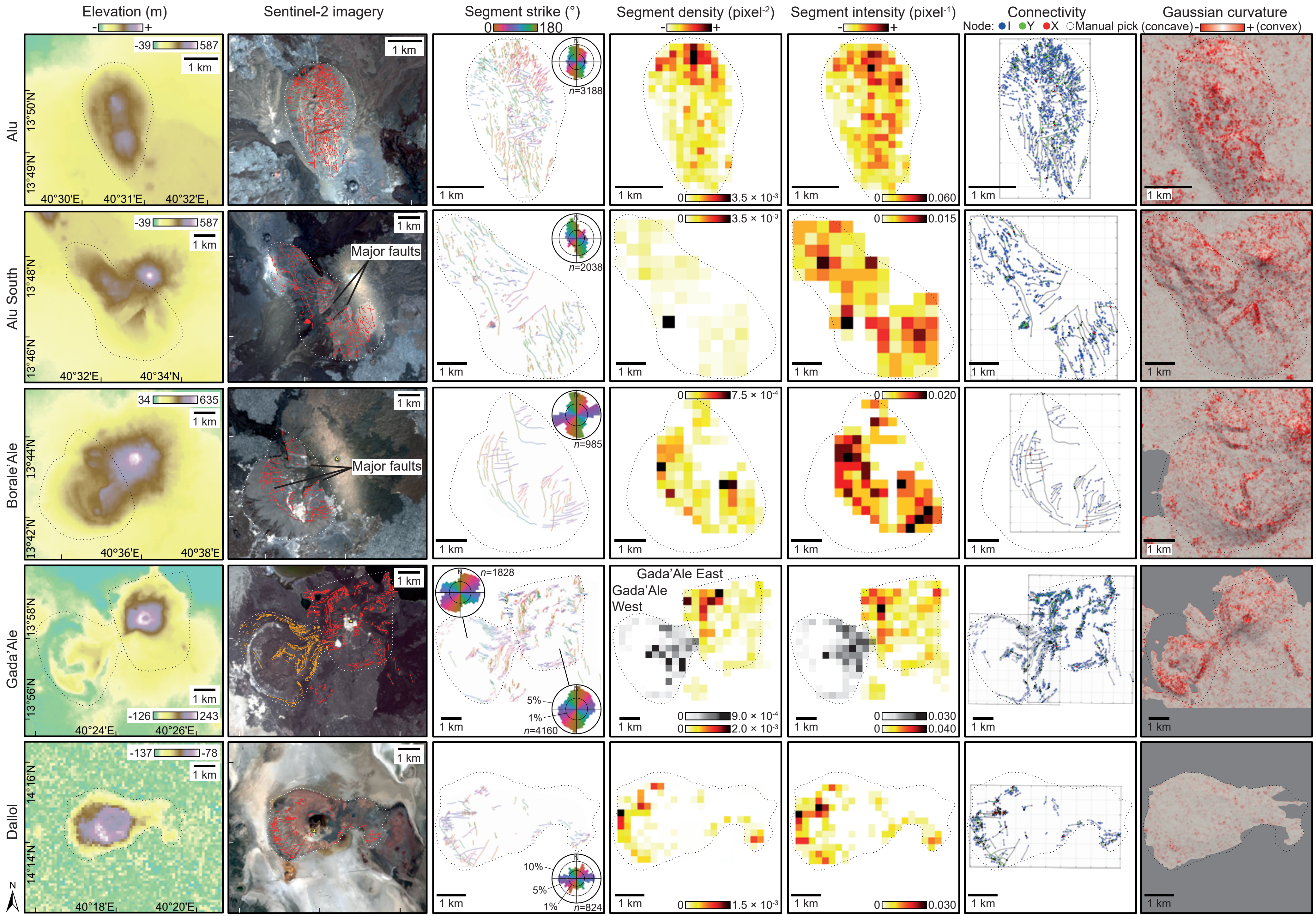

Elevation (m)
Sentinel-2 imagery
Segment strike (°)
0
180
Segment density (pixel^{-2})
Segment intensity (pixel^{-1})
Connectivity
Node: I Y X Manual pick
Gaussian curvature
(concave)
(convex)
Alu
Alu South
Borale'Ale
Gada'Ale
Dallol
-39
587
34
635
-126
243
-137
-78
1 km
13°50'N
13°49'N
40°30'E
40°31'E
40°32'E
13°48'N
13°46'N
40°32'E
40°34'N
13°44'N
13°42'N
40°36'E
40°38'E
13°58'N
13°56'N
40°24'E
40°26'E
14°16'N
14°14'N
40°18'E
40°20'E
N
Major faults
n=3188
n=2038
n=985
n=1828
n=4160
n=824
5%
1%
10%
0
3.5 × 10^{-3}
7.5 × 10^{-4}
9.0 × 10^{-4}
2.0 × 10^{-3}
1.5 × 10^{-3}
0.060
0.015
0.020
0.030
0.040
Gada'Ale East
Gada'Ale West

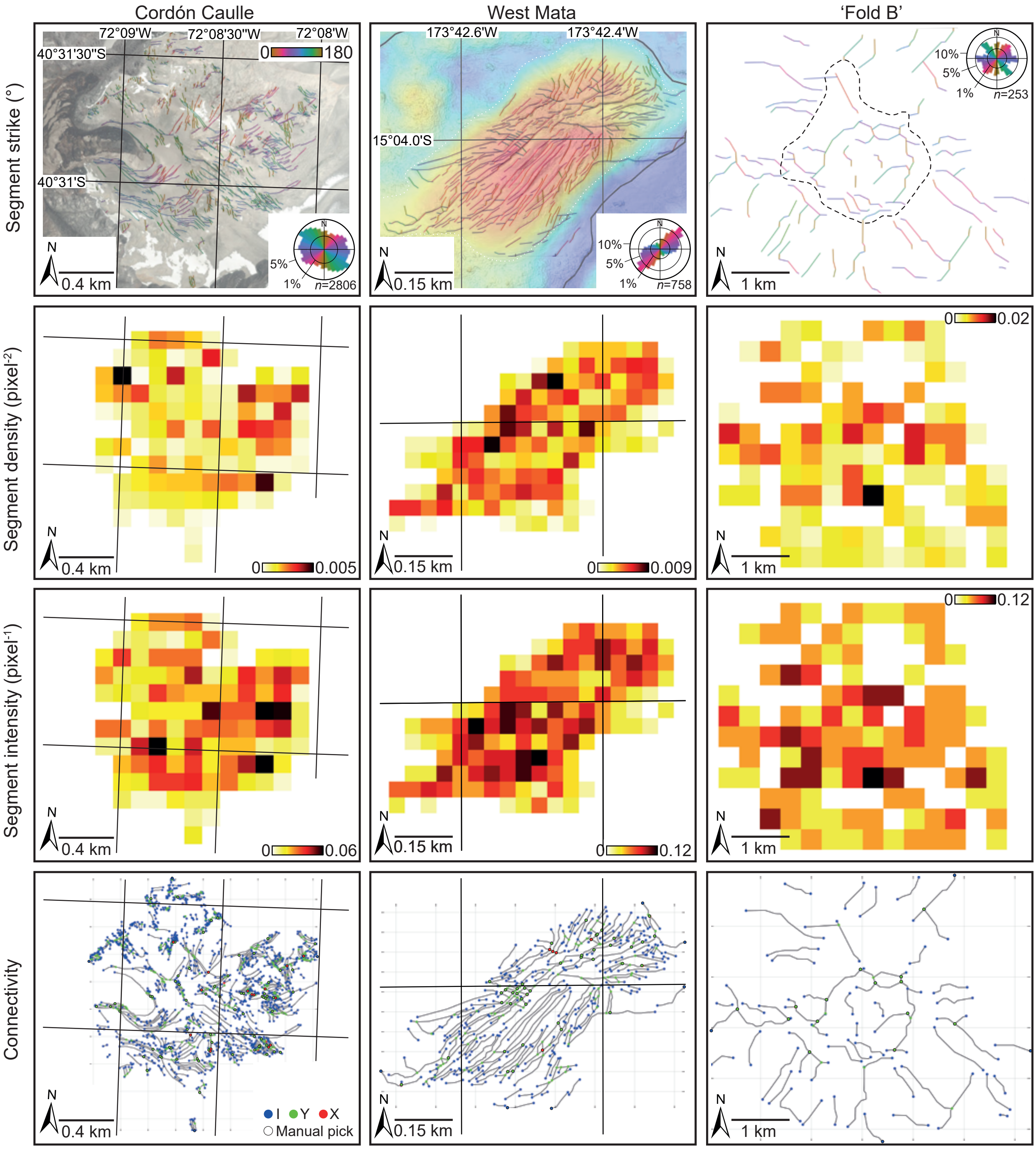

Cordón Caulle
West Mata
'Fold B'
Segment strike (°)
Segment density (pixel-2)
Segment intensity (pixel-1)
Connectivity
72°09'W
72°08'30"W
72°08'W
40°31'30"S
40°31'S
0
180
173°42.6'W
173°42.4'W
15°04.0'S
N
0.4 km
0.15 km
1 km
5%
1%
n=2806
10%
n=758
n=253
0.005
0.009
0.02
0.06
0.12
I
Y
X
Manual pick

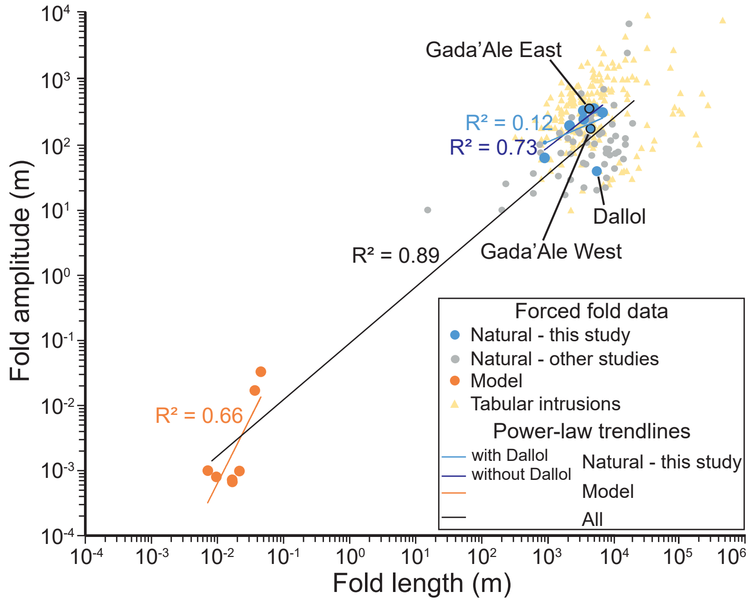

Fold amplitude (m)
Fold length (m)
Gada'Ale East
Gada'Ale West
Dallol
R² = 0.12
R² = 0.73
R² = 0.89
R² = 0.66
Forced fold data
Natural - this study
Natural - other studies
Model
Tabular intrusions
Power-law trendlines
with Dallol
without Dallol
Natural - this study
Model
All

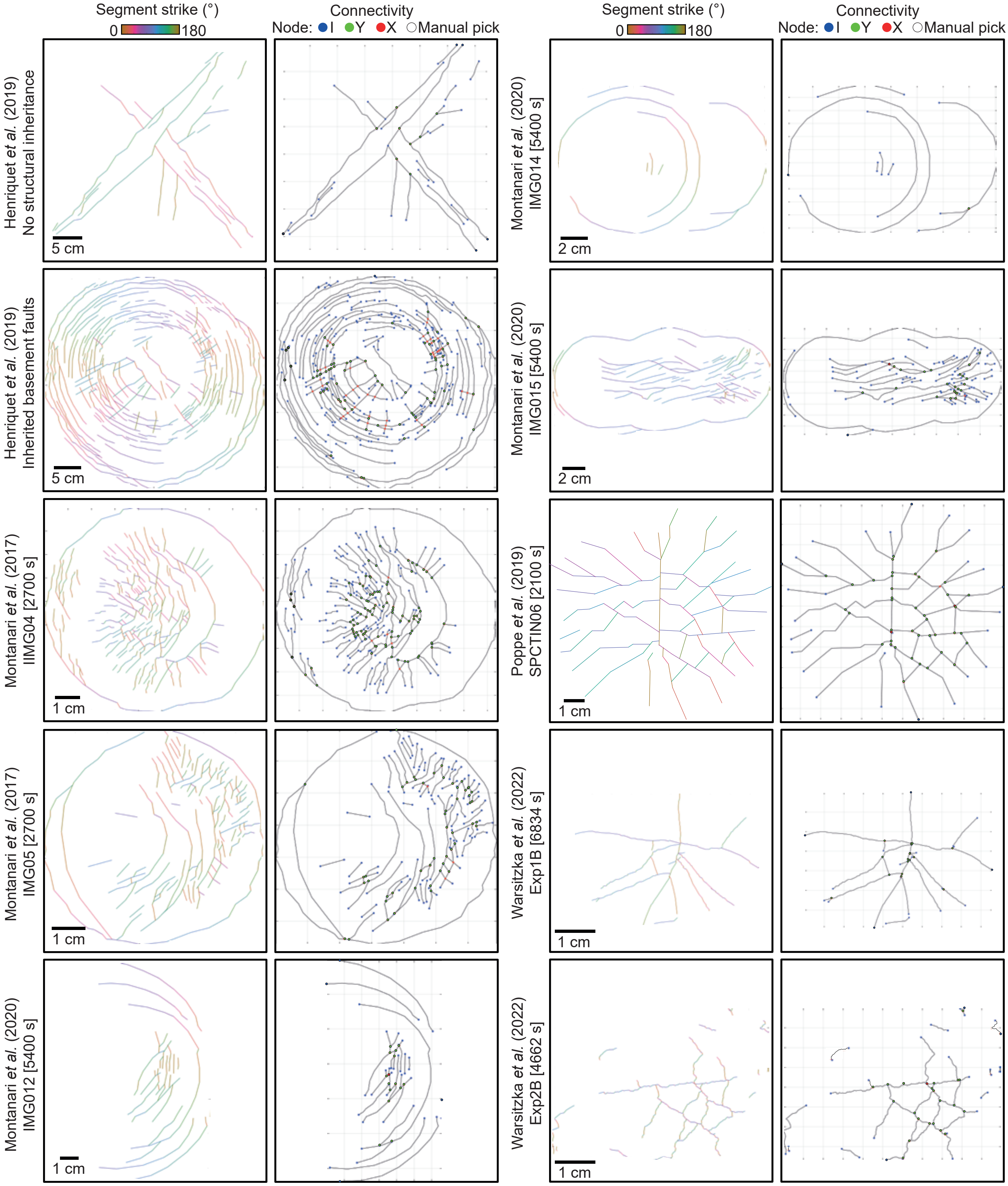

Segment strike (°)
0
180
Connectivity
Node: I Y X Manual pick
Henriquet et al. (2019)
No structural inheritance
5 cm
Henriquet et al. (2019)
Inherited basement faults
5 cm
Montanari et al. (2017)
IIMG04 [2700 s]
1 cm
Montanari et al. (2017)
IMG05 [2700 s]
1 cm
Montanari et al. (2020)
IMG012 [5400 s]
1 cm
Montanari et al. (2020)
IMG014 [5400 s]
2 cm
Montanari et al. (2020)
IMG015 [5400 s]
2 cm
Poppe et al. (2019)
SPCTIN06 [2100 s]
1 cm
Warsitzka et al. (2022)
Exp1B [6834 s]
1 cm
Warsitzka et al. (2022)
Exp2B [4662 s]
1 cm

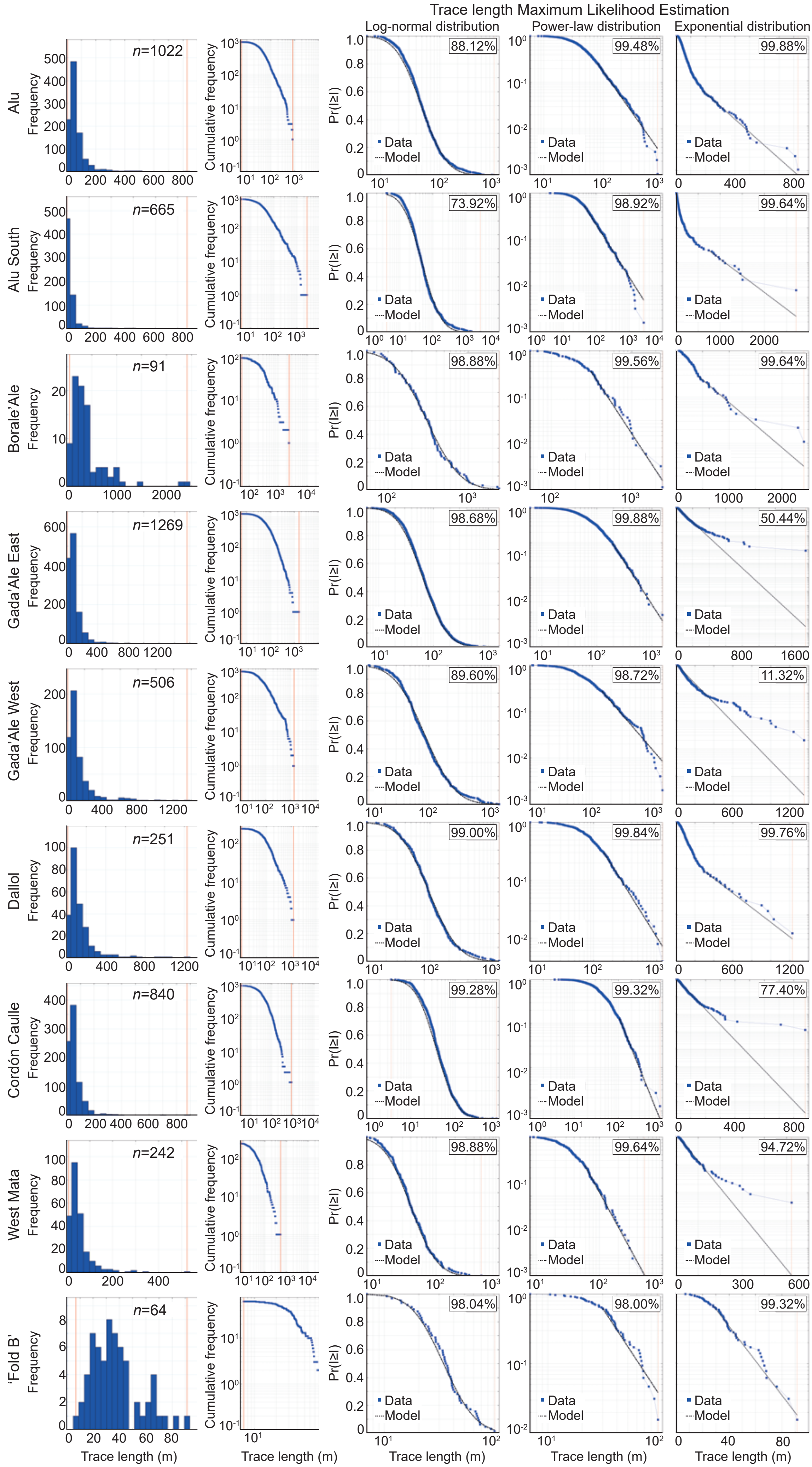

Trace length Maximum Likelihood Estimation
Log-normal distribution
Power-law distribution
Exponential distribution
Alu
n=1022
88.12%
99.48%
99.88%
Alu South
n=665
73.92%
98.92%
99.64%
Borale'Ale
n=91
98.88%
99.56%
99.64%
Gada'Ale East
n=1269
98.68%
99.88%
50.44%
Gada'Ale West
n=506
89.60%
98.72%
11.32%
Dallol
n=251
99.00%
99.84%
99.76%
Cordón Caulle
n=840
99.28%
99.32%
77.40%
West Mata
n=242
98.88%
99.64%
94.72%
'Fold B'
n=64
98.04%
98.00%
99.32%
Frequency
Cumulative frequency
Pr(l≥l)
Data
Model
Trace length (m)

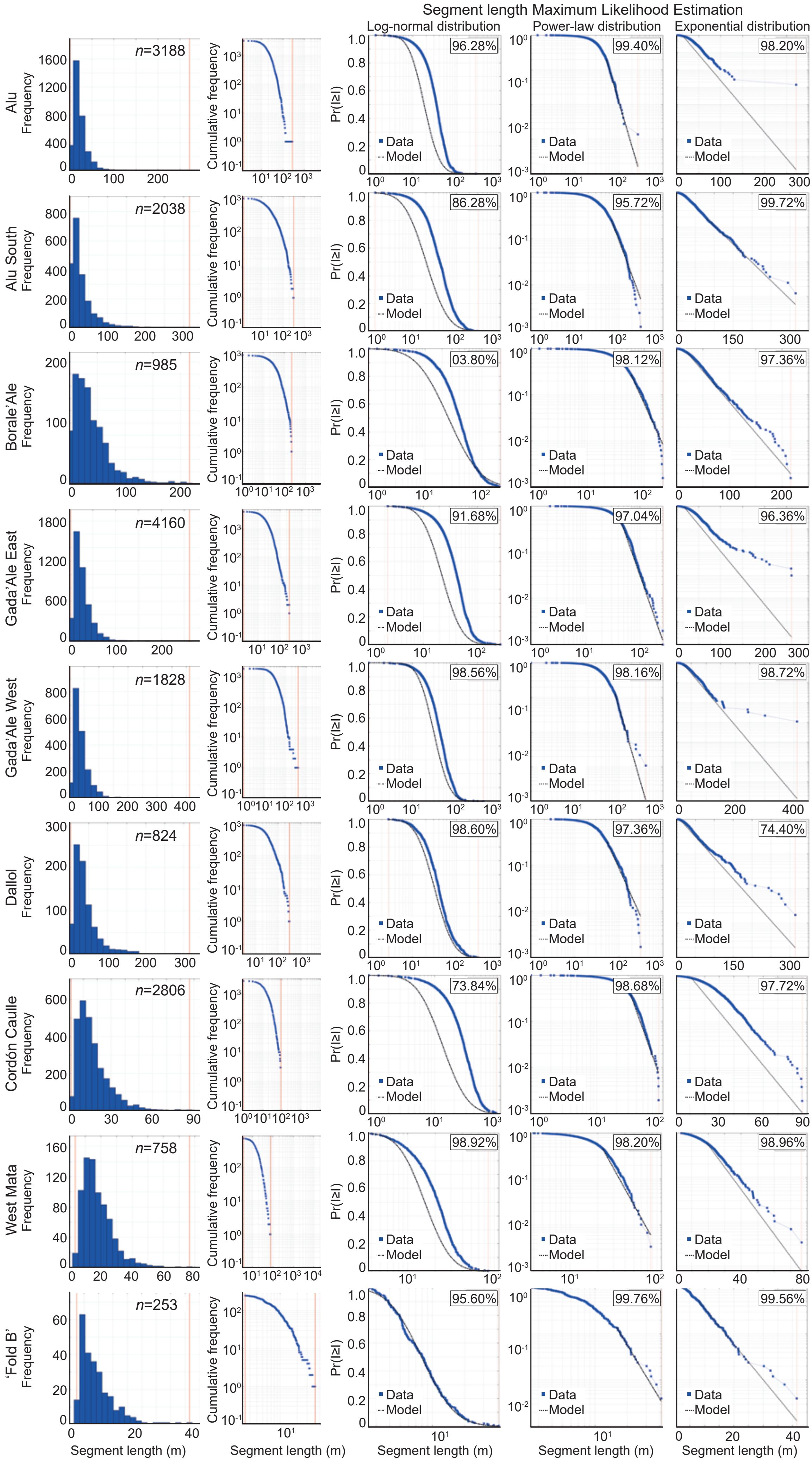

Segment length Maximum Likelihood Estimation
Log-normal distribution
Power-law distribution
Exponential distribution
Alu
n=3188
96.28%
99.40%
98.20%
Alu South
n=2038
86.28%
95.72%
99.72%
Borale'Ale
n=985
03.80%
98.12%
97.36%
Gada'Ale East
n=4160
91.68%
97.04%
96.36%
Gada'Ale West
n=1828
98.56%
98.16%
98.72%
Dallol
n=824
98.60%
97.36%
74.40%
Cordón Caulle
n=2806
73.84%
98.68%
97.72%
West Mata
n=758
98.92%
98.20%
98.96%
'Fold B'
n=253
95.60%
99.76%
99.56%
Frequency
Cumulative frequency
Pr(≥l)
Data
Model
Segment length (m)

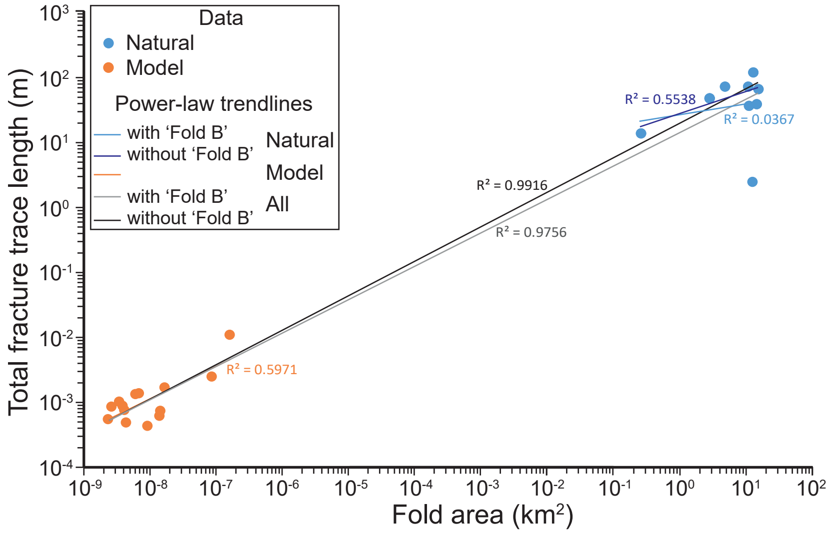

Data
Natural
Model
Power-law trendlines
with 'Fold B'
without 'Fold B'
Natural
Model
with 'Fold B'
without 'Fold B'
All
$R^2 = 0.5538$
$R^2 = 0.0367$
$R^2 = 0.9916$
$R^2 = 0.9756$
$R^2 = 0.5971$
Total fracture trace length (m)
Fold area (km^2)
10^3
10^2
10^1
10^0
10^{-1}
10^{-2}
10^{-3}
10^{-4}
10^{-9}
10^{-8}
10^{-7}
10^{-6}
10^{-5}
10^{-4}
10^{-3}
10^{-2}
10^{-1}
10^0
10^1
10^2

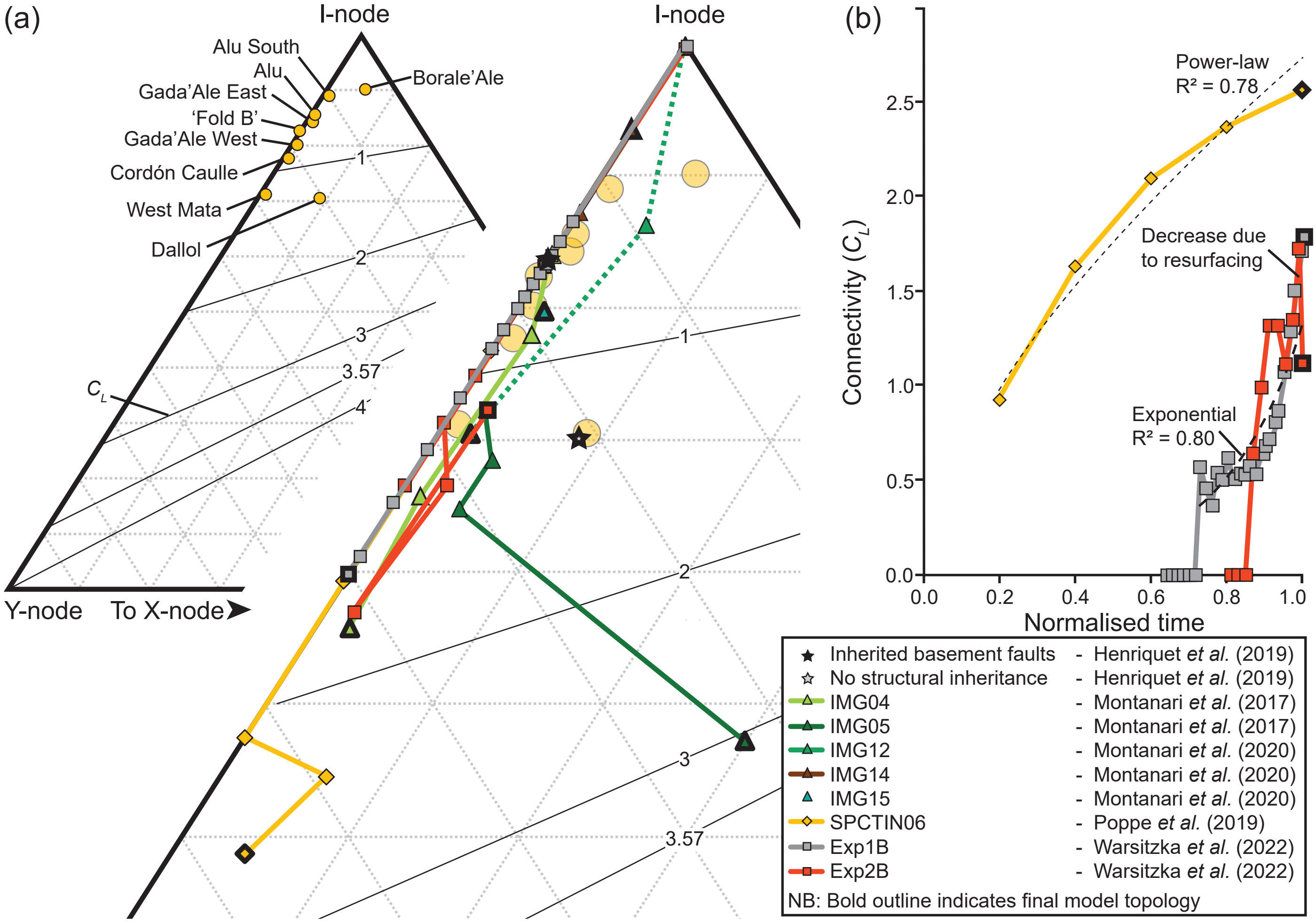

(a)
I-node
Alu South
Alu
Gada'Ale East
'Fold B'
Gada'Ale West
Cordón Caulle
West Mata
Dallol
Borale'Ale
C_L
Y-node
To X-node
(b)
Power-law
R² = 0.78
Decrease due to resurfacing
Exponential
R² = 0.80
Connectivity (C_L)
Normalised time
Inherited basement faults - Henriquet et al. (2019)
No structural inheritance - Henriquet et al. (2019)
IMG04 - Montanari et al. (2017)
IMG05 - Montanari et al. (2017)
IMG12 - Montanari et al. (2020)
IMG14 - Montanari et al. (2020)
IMG15 - Montanari et al. (2020)
SPCTIN06 - Poppe et al. (2019)
Exp1B - Warsitzka et al. (2022)
Exp2B - Warsitzka et al. (2022)
NB: Bold outline indicates final model topology

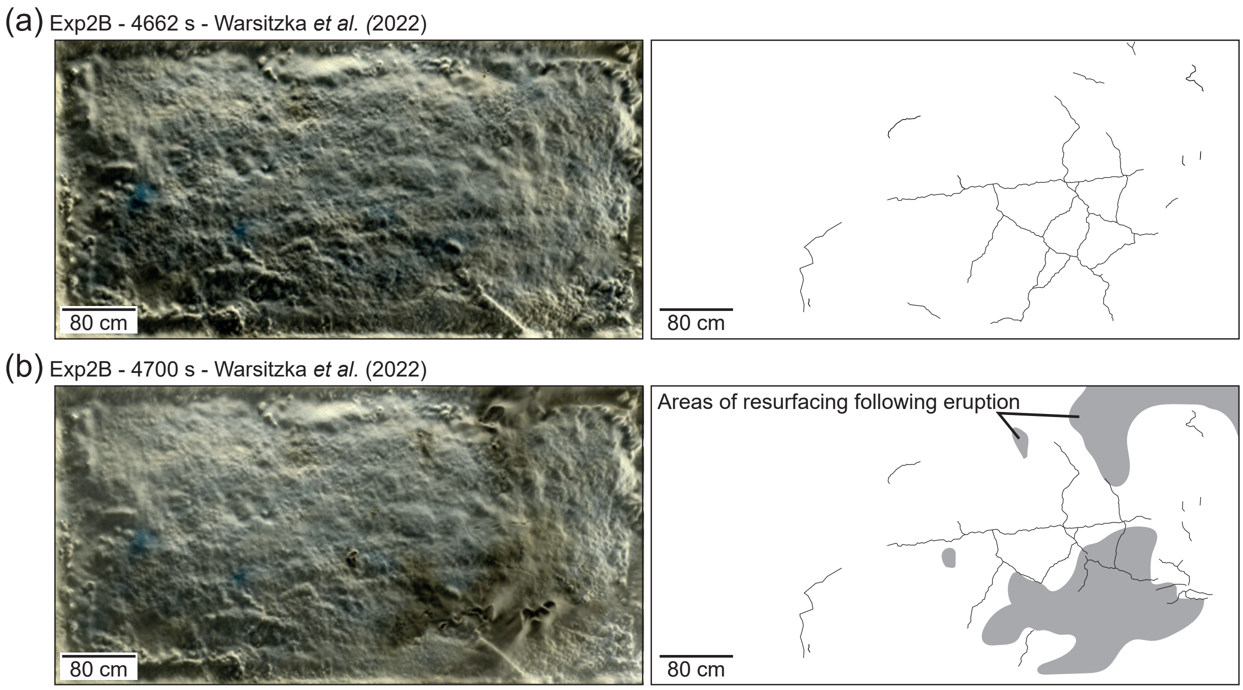
(a) Exp2B - 4662 s - Warsitzka et al. (2022)
80 cm
80 cm
(b) Exp2B - 4700 s - Warsitzka et al. (2022)
80 cm
Areas of resurfacing following eruption
80 cm